

# Cosmological Constraints from the Large Scale Weak Lensing of SDSS MaxBCG Clusters

Ying Zu<sup>1\*</sup>, David H. Weinberg<sup>1</sup>, Eduardo Rozo<sup>2,3</sup>, Erin S. Sheldon<sup>4</sup>, Jeremy L. Tinker<sup>5</sup>,  
Matthew R. Becker<sup>3,6</sup>

<sup>1</sup> Department of Astronomy and CCAPP, The Ohio State University, 140 W. 18th Avenue, Columbus, OH 43210, USA

<sup>2</sup> Einstein Fellow, Department of Astronomy & Astrophysics, The University of Chicago, Chicago, IL 60637, USA

<sup>3</sup> Kavli Institute for Cosmological Physics, 5640 South Ellis Avenue, The University of Chicago, Chicago, IL 60637, USA

<sup>4</sup> Brookhaven National Laboratory, Bldg 510, Upton, New York 11973, USA

<sup>5</sup> Center for Cosmology and Particle Physics, Department of Physics, New York University, USA

<sup>6</sup> Department of Physics, 5720 S. Ellis Avenue, The University of Chicago, Chicago, IL 60637, USA

20 February 2022

## ABSTRACT

We derive constraints on the matter density  $\Omega_m$  and the amplitude of matter clustering  $\sigma_8$  from measurements of large scale weak lensing (projected separation  $R = 5 - 30h^{-1}\text{Mpc}$ ) by clusters in the Sloan Digital Sky Survey MaxBCG catalog. The weak lensing signal is proportional to the product of  $\Omega_m$  and the cluster–mass correlation function  $\xi_{\text{cm}}$ . With the relation between optical richness and cluster mass constrained by the observed cluster number counts, the predicted lensing signal increases with increasing  $\Omega_m$  or  $\sigma_8$ , with mild additional dependence on the assumed scatter between richness and mass. The dependence of the signal on scale and richness partly breaks the degeneracies among these parameters. We incorporate external priors on the richness–mass scatter from comparisons to X-ray data and on the shape of the matter power spectrum from galaxy clustering, and we test our adopted model for  $\xi_{\text{cm}}$  against N-body simulations. Using a Bayesian approach with minimal restrictive priors, we find  $\sigma_8(\Omega_m/0.325)^{0.501} = 0.828 \pm 0.049$ , with marginalized constraints of  $\Omega_m = 0.325^{+0.086}_{-0.067}$  and  $\sigma_8 = 0.828^{+0.111}_{-0.097}$ , consistent with constraints from other MaxBCG studies that use weak lensing measurements on small scales ( $R \leq 2h^{-1}\text{Mpc}$ ). The  $(\Omega_m, \sigma_8)$  constraint is consistent with and orthogonal to the one inferred from WMAP CMB data, reflecting agreement with the structure growth predicted by General Relativity for a  $\Lambda\text{CDM}$  cosmological model. A joint constraint assuming  $\Lambda\text{CDM}$  yields  $\Omega_m = 0.298^{+0.019}_{-0.020}$  and  $\sigma_8 = 0.831^{+0.020}_{-0.020}$ . For these parameters and our best-fit scatter we obtain a tightly constrained mean richness–mass relation of MaxBCG clusters,  $N_{200} = 25.4(M/3.61 \times 10^{14}h^{-1}M_\odot)^{0.74}$ , with a normalization uncertainty of 1.5%. Our cosmological parameter errors are dominated by the statistical uncertainties of the large scale weak lensing measurements, which should shrink sharply with current and future imaging surveys.

**Key words:** methods: statistical — cosmology: cosmological parameters — cosmology: large-scale structure of Universe

## 1 INTRODUCTION

The most fundamental question about the origin of cosmic acceleration is whether it arises from a new energy component or from a modification of General Relativity (GR) on cosmological scales. A general strategy to address this question is to compare the growth of cosmic structure — as measured, e.g., by cosmic shear, redshift–space distortions of galaxy clustering, or the

abundance of galaxy clusters as a function of mass — to the predictions of a GR+dark energy model constrained by geometrical probes such as Type Ia supernovae and baryon acoustic oscillations (BAO). In particular, one can compare measurements of the matter density  $\Omega_m$  and the present–day amplitude of matter clustering, characterized by  $\sigma_8$ , the rms matter fluctuation in  $8h^{-1}\text{Mpc}$  spheres, to the values expected from extrapolating cosmic microwave background (CMB) anisotropies forward from recomb-

\* E-mail: yingzu@astronomy.ohio-state.edu

nation to  $z = 0$ .<sup>1</sup> Cosmological studies with clusters traditionally use mass proxies derived from X-ray or Sunyaev–Zel’dovich (SZ; Sunyaev & Zeldovich 1972) measurements to constrain the cluster mass function  $dn/dM$  (see Allen et al. 2011 for a review). In an alternative approach, Sheldon et al. (2009; hereafter S09) used stacked weak lensing (WL) to measure the average mass profiles around clusters in the MaxBCG catalog (Koester et al. 2007) derived from the Sloan Digital Sky Survey (SDSS; York et al. 2000), detecting correlated mass from scales of  $0.1h^{-1}\text{Mpc}$  to  $30h^{-1}\text{Mpc}$ . Rozo et al. (2010; hereafter R10) used the S09 measurements to constrain the mean relation between optical richness and virial mass for MaxBCG clusters, and they combined this relation with the abundance of clusters as a function of richness to constrain  $\Omega_m$  and  $\sigma_8$ . (For a general review of this approach in the context of cluster cosmology, see §6 of Weinberg et al. 2012.) In this paper we again target  $\Omega_m$  and  $\sigma_8$  with MaxBCG clusters, but we use the *large scale* S09 measurements, from projected separations of  $5\text{--}30h^{-1}\text{Mpc}$ .

Roughly speaking, stacked weak lensing measures the product of the matter density  $\Omega_m$  and the cluster–mass cross–correlation function  $\xi_{\text{cm}}(r)$ . More precisely, given knowledge of the distances to lensing clusters and background sources, the mean tangential shear profile of clusters measures the excess surface density profile  $\Delta\Sigma(R)$ , which is related to the 3-d  $\xi_{\text{cm}}(r)$  via

$$\begin{aligned} \Delta\Sigma(R) &= \Omega_m \rho_c \frac{2}{R^2} \int_0^R \int_{-\infty}^{+\infty} r_p \xi_{\text{cm}} \left( \sqrt{r_p^2 + r_z^2} \right) dr_z dr_p \\ &- \Omega_m \rho_c \int_{-\infty}^{+\infty} \xi_{\text{cm}} \left( \sqrt{R^2 + r_z^2} \right) dr_z \end{aligned} \quad (1)$$

(see § 2 for further details). We can understand how large scale  $\Delta\Sigma(R)$  measurements constrain  $\Omega_m$  and  $\sigma_8$  by considering the simple case in which optical richness is perfectly correlated with cluster mass, so that a sample of clusters above a richness threshold corresponds to a sample above a mass threshold that has the same comoving space density  $\bar{n}$  (where, for simplicity, we consider a sample at fixed redshift). For a given cosmological model, one can predict the matter correlation function  $\xi_{\text{mm}}(r)$  and the bias factor  $b_c(\bar{n})$  of halos with space density  $\bar{n}$ , and thus the cluster–mass correlation function, which is  $\xi_{\text{cm}}(r) = b_c(\bar{n})\xi_{\text{mm}}(r)$  on scales in the linear regime. Raising  $\Omega_m$  with all other quantities held fixed raises the predicted  $\Delta\Sigma(R)$  proportionally. Raising  $\sigma_8$  increases  $\xi_{\text{mm}} \propto \sigma_8^2$  and thus increases  $\xi_{\text{cm}}(r)$ , but there is a partly compensating decline in  $b_c(\bar{n})$ . In the limit of very rare, very highly biased peaks,  $b_c(\bar{n}) \propto \sigma_8^{-1}$ , yielding  $\Delta\Sigma(R) \propto \Omega_m \sigma_8$ , but for the space densities of typical cluster samples  $b_c(\bar{n})$  drops more slowly than  $\sigma_8^{-1}$ . Thus, the combination of cluster abundance measurements, which determine  $\bar{n}$ , and large scale weak lensing measurements, which determine  $\Delta\Sigma(R)$ , constrains a parameter combination  $\sigma_8 \Omega_m^\gamma$  with  $\gamma < 1$ . In practice, we will use bins of cluster richness instead of a single sample above a threshold, and the  $\sigma_8$ –dependence of  $\xi_{\text{cm}}(r)$  is different in the linear and mildly non-linear regimes, so there is some leverage to break degeneracy between  $\Omega_m$  and  $\sigma_8$ .

The simplifications of this description point up several complications that must be addressed in our analysis. First, the measurements of  $\Delta\Sigma(R)$  have systematic uncertainties related to the photometric redshifts of the sources and shear calibration. Second, optical richness is a mass indicator with substantial scatter, which

makes the bias of clusters in richness bins different from that of mass bins with the same space density. The two principal “nuisance parameters” in our statistical analysis are  $\beta$ , an overall scaling of the  $\Delta\Sigma(R)$  measurements to allow for systematic uncertainty, and  $\sigma_{\ln N_{200}|M}$ , the logarithmic scatter in richness at fixed mass. We discuss these nuisance parameters and the priors we adopt on them in § 3. We also adopt a prior on the shape of the matter power spectrum, so that a value of  $\sigma_8$  specifies the full shape of  $\xi_{\text{mm}}(r)$ . The inference of comoving space densities itself depends on  $\Omega_m$ , which affects the volume element transformation between comoving distances and observable angles and redshifts. Incompleteness and contamination of the cluster sample can also affect the inferred space densities and/or bias the estimate of  $\Delta\Sigma(R)$ , so they must also be accounted in the analysis. Despite these complications, we find that our constraints are limited by the statistical errors of the weak lensing measurements rather than systematic uncertainties.

A complete cosmological analysis of cluster weak lensing would employ  $\Delta\Sigma(R)$  measurements over the full range of observed scales. Here we restrict our analysis to  $R \geq 5h^{-1}\text{Mpc}$ , in part to avoid the regime where theoretical predictions of  $\xi_{\text{cm}}(r)$  are uncertain, and in part to keep our results complementary to those of R10, who use the small scale ( $R \lesssim 2h^{-1}\text{Mpc}$ ) S09 measurements to calibrate their determination of the cluster mass function. One important systematic for interpretation of the small scale measurements is the impact of cluster mis-centering, which must be estimated from simulations of the cluster population and cluster finding technique (e.g. Johnston et al. 2007; George et al. 2012). One advantage of the approach in this paper is that mis-centering has negligible impact at the large scales that we employ.

In the following section we briefly review our input data, the MaxBCG cluster catalog and the S09 weak lensing measurements. Section 3 presents our analysis method in detail, including the model parameters and priors and the procedure for computing the likelihood of the data given these parameters. Section 4 tests our analytic models for  $\Delta\Sigma(R)$  (a modified version of that proposed by Hayashi & White 2008, hereafter HW08) against numerical simulations, and it uses simple mock data sets to test other aspects of our analysis procedures. Section 5 presents our cosmological constraints and compares them to those from other cluster analyses and from CMB data. We address systematic uncertainties in §6. We close, in §7, with a summary of our findings and a discussion of future prospects. The reader in a hurry can get an overview of the paper from Fig. 1, which compares our best-fit model to our input data, Fig. 7, which shows how the  $\Delta\Sigma(R)$  prediction depends on model parameters, and Fig. 9, which presents our derived constraints on  $\Omega_m$  and  $\sigma_8$ .

## 2 DATA

### 2.1 Cluster Catalog and Number Counts

The MaxBCG cluster catalog (Koester et al. 2007) consists of 13,823 clusters identified from the imaging data of the SDSS Data Release 4 (DR4; Adelman-McCarthy et al. 2006). The clusters are selected as spatial overdensities of red galaxies, which form a tight E/S0 ridgeline in the color–magnitude diagram. Each cluster is assigned a richness measure  $N_{200}$ , defined as the number of red–sequence galaxies with  $L > 0.4L_*$  in the  $i$ -band within a scaled radius  $R_{200}$  such that the galaxy density interior to that radius is 200 times the mean galaxy density. The tight relation between the ridgeline color and redshift also allows an accurate photometric

<sup>1</sup> We define  $h \equiv H_0/(100 \text{ km s}^{-1} \text{Mpc}^{-1})$  where  $H_0$  is the Hubble parameter at  $z = 0$ .

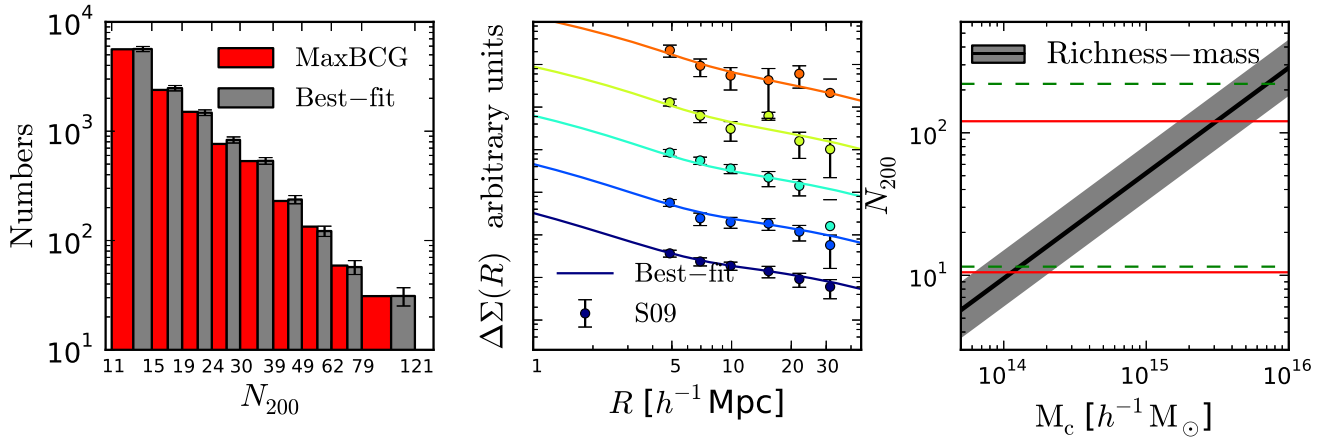


**Figure 1.** Comparison between observables used in the analysis and the best-fit model predictions. Left panel: Cluster number counts from the MaxBCG sample (dark/red histograms) and the best-fit model prediction (light histograms with errorbars). Middle panel: Stacked surface density contrast profiles of five richness bins measured by S09 (solid circles with errorbars) and predicted by the best-fit model (solid curves), multiplied by a different constant for each bin to avoid crowding. Errorbars in the left and middle panels correspond to the square root of the diagonal terms in the covariance matrix. Right panel: Mean richness–mass relation (thick solid line) and intrinsic scatter (gray shaded stripe) of the best-fit model. Solid and dashed horizontal lines bracket the richness ranges associated with the cluster samples we used for the number counts and  $\Delta\Sigma(R)$ , respectively.

redshift estimate for each cluster ( $\Delta z \simeq 0.01$ ). Tests against mock catalogs suggest MaxBCG is  $\sim 90\%$  complete and pure for clusters with masses  $\geq 10^{14} h^{-1} M_{\odot}$ , and 95% for higher mass clusters (Rozo et al. 2007a). The MaxBCG catalog is nearly volume-limited in the redshift range between 0.1 and 0.3 over 7398 deg<sup>2</sup>. The large volume and dynamic range in mass make it well suited to our cosmological analysis.

For better control on purity and completeness, we only keep 10,815 MaxBCG clusters (78% of total) with  $N_{200} > 11$  for the abundance measurement. Since there are only 5 clusters with  $N_{200} > 120$  but they span a large richness range to  $N_{200}^{\max} = 188$ , we need to model the number counts for clusters with  $N_{200}$  below and above 120 separately. We will describe the difference of their treatments in our likelihood model in § 3.2.

For the clusters with  $N_{200} \in \{11 \dots 120\}$ , Table 1 gives our richness binning, and the red histograms in the left panel of Fig. 1 (discussed further below) show the measured number counts in those bins. When predicting these numbers for a set of model parameters, we integrate over redshift and account for scatter between photometric and true redshift, with a survey area of 7398 deg<sup>2</sup>. To a good approximation, the predicted counts are what one would obtain using the halo mass function at  $z = 0.23$  and the comoving volume from  $z = 0.1$  to  $z = 0.3$ .

## 2.2 Large Scale Cluster Weak Lensing Measurements

We take our large scale weak lensing measurements from S09, who measured the mean tangential shear profiles  $\gamma_T(R)$  of source galaxies around lens clusters in bins of richness. The area of the imaging data used for this analysis is somewhat smaller than the 7398 deg<sup>2</sup> used for the number counts. The mean tangential shear is then converted to the mean excess surface density profile  $\Delta\Sigma(R)$  for each richness bin,

$$\Delta\Sigma(R) \equiv \bar{\Sigma}(<R) - \bar{\Sigma}(R) = \gamma_T(R) \times \Sigma_{\text{crit}}, \quad (2)$$

where  $\bar{\Sigma}(R)$  is the azimuthally averaged density at projected radius  $R$  and  $\bar{\Sigma}(<R)$  is the mean surface density *interior* to  $R$  (see,

e.g. Miralda-Escude 1991; Sheldon et al. 2004). The critical surface density  $\Sigma_{\text{crit}}$  above is defined to be

$$\Sigma_{\text{crit}} = \frac{c^2}{4\pi G} \frac{D_S}{D_{LS} D_L}, \quad (3)$$

where  $D_S$ ,  $D_L$ , and  $D_{LS}$  are the angular diameter distances from the observer to the source, from the observer to the lens, and between the lens and source, respectively. To calculate  $\Sigma_{\text{crit}}$ , S09 estimated  $D_S$  and  $D_{LS}$  using the photo- $z$ 's of source galaxies, so any uncertainties in the photo- $z$  estimates affect the measurements of  $\Delta\Sigma(R)$ , as we will describe in § 3.1. The values of  $\Sigma_{\text{crit}}$  are computed for a spatially flat universe with  $\Omega_m = 0.28$  and a cosmological constant. Over our redshift range, the impact of varying this assumption is negligible compared to the statistical errors, so we do not adjust  $\Sigma_{\text{crit}}$  when fitting cosmological parameters.

While the signal-to-noise ratio of  $\Delta\Sigma(R)$  for each cluster is small, S09 stacked the signals among all clusters in each richness bin to obtain average  $\Delta\Sigma(R)$  profiles. The stacked signal was detected from the inner halo ( $25 h^{-1} \text{kpc}$ ) well into the surrounding large scale structure ( $30 h^{-1} \text{Mpc}$ ). As mentioned in the introduction, the small scale measurements were used by R10 for their constraints, and we hope to employ the large scales by interpreting  $\Delta\Sigma(R)$  as a measure for  $\Omega_m \xi_{\text{cm}}$ .

Table 2 summarizes the richness binning for  $\Delta\Sigma(R)$ , and the solid circles in the middle panel of Fig. 1 show the measured  $\Delta\Sigma(R)$  on large scales. Errorbars are derived from jackknife re-sampling (see § 3.2 below) and are correlated between points. We take our data values for  $\Delta\Sigma(R)$  from table 1 of S09 with one important correction. As first noted by Mandelbaum et al. (2008), the weak lensing signal in S09 appears to be diluted because of photometric redshift errors that incorrectly locate some foreground galaxies (which cannot be lensed by the clusters) behind the clusters. Rozo et al. (2009) estimated that the original S09 measurements of  $\Delta\Sigma(R)$  should be multiplied by factor 1.18, with uncertainty of 0.04. We adopt this factor of 1.18 to scale the original S09  $\Delta\Sigma(R)$  and its associated error matrix up as the actual data for the analysis, and we refer to these scaled data as the “S09 measurements” in the rest of the paper.

**Table 1.** Richness bins for the abundance data. The average mass and bias of clusters in each bin are computed from the best-fit MaxBCG+WMAP7 joint model.

Richness	No. of Clusters $N_i$	$\langle M_{200m} \rangle_i [h^{-1} M_\odot]$	$\langle b \rangle_i$
11-14	5167	$0.997 \times 10^{14}$	2.373
15-18	2387	$1.404 \times 10^{14}$	2.696
19-23	1504	$1.857 \times 10^{14}$	3.010
24-29	765	$2.417 \times 10^{14}$	3.359
30-38	533	$3.153 \times 10^{14}$	3.772
39-48	230	$4.108 \times 10^{14}$	4.260
49-61	134	$5.200 \times 10^{14}$	4.769
62-78	59	$6.556 \times 10^{14}$	5.353
79-120	31	$8.627 \times 10^{14}$	6.170

### 3 ANALYSIS

To obtain constraints on  $\Omega_m$  and  $\sigma_8$ , we adopt a Bayesian approach with a minimal set of restrictive priors on nuisance parameters. To facilitate the analysis, we also utilize information known from other experiments, specifically, the shape of the linear power spectrum and the scatter of cluster masses at given richness, as priors into our analysis. Details on the model parameters, likelihood components, and the prior specifications can be found below.

#### 3.1 Model Parameters

We assume a flat  $\Lambda$ CDM cosmology and infer the values of  $\Omega_m$  and  $\sigma_8$ , along with other nuisance parameters. Any deviation from the flat  $\Lambda$ CDM+GR assumption would manifest itself as inconsistent constraints on  $\Omega_m$  and  $\sigma_8$  compared to expectations from the CMB, because of growth that differs from predictions of the GR+cosmological constant model. Since we introduce the shape of the linear power spectrum  $P_{\text{lin}}(k)$  inferred from galaxy redshift surveys as a prior, we do not assume specific values for the tilt of the primordial power spectrum  $n_s$ , the baryon density  $\Omega_b h^2$  and the neutrino mass  $\Omega_\nu h^2$ , but only require them to be consistent with the input power spectrum shape and the output constraints on  $\Omega_m$  and  $\sigma_8$ . Our analysis is also independent of the assumed value of the Hubble parameter  $h$ , as both the power spectrum shape and the weak lensing shear are measured from galaxies and clusters in the local universe, so that all distances are in units of  $h^{-1}$  Mpc. While the  $P(k)$  shape is determined very well on the scales that are relevant to galaxies and clusters (Reid et al. 2010, hereafter Reid10), it could swing away on other scales. We therefore allow rotational freedom in the  $P(k)$  shape by introducing a modification to the overall tilt as another parameter  $\Delta n_s$ , representing residual uncertainty in the  $P(k)$  shape. The final linear power spectrum  $P_{\text{lin}}(k)$  is then  $\propto P_{\text{Reid10}}(k) k^{\Delta n_s}$ , normalized accordingly by the input  $\sigma_8$ . We comment more on the  $P(k)$  shape in § 4.3.

Following R10, we assume that the mean cluster richness–mass relation is a power-law, parameterized by two mean log-richnesses,  $\ln \bar{N}_1$  and  $\ln \bar{N}_2$ , at  $M_1 = 1.3 \times 10^{14} h^{-1} M_\odot$  and  $M_2 = 1.3 \times 10^{15} h^{-1} M_\odot$ , respectively. We investigate the effect of allowing deviation from a power-law in § 6. To go from the *expected* mean richness of a cluster of mass  $M$  to the actual observed richness, we assume a log–normal distribution with a constant scatter  $\sigma_{\ln N_{200}|M}$  across all cluster masses. Note that, unlike R10, we use mass unit  $h^{-1} M_\odot$  rather than  $M_\odot$  throughout the analysis, in accordance with our choice of distance units to avoid dependence on  $h$ . The right panel of Fig. 1 shows the richness–

**Table 2.** Richness bins for the stacked  $\Delta\Sigma(R)$  measurements. The average mass and bias of clusters in each bin are computed from the best-fit MaxBCG+WMAP7 joint model.

Richness	No. of Clusters $N_j$	$\langle M_{200m} \rangle_j [h^{-1} M_\odot]$	$\langle b \rangle_j$
12-17	5651	$1.166 \times 10^{14}$	2.511
18-25	2269	$1.860 \times 10^{14}$	3.010
26-40	1021	$2.918 \times 10^{14}$	3.641
41-70	353	$4.822 \times 10^{14}$	4.591
71+	55	$8.459 \times 10^{14}$	6.093

mass relation predicted by our best-fit model, with  $\ln \bar{N}_1 = 2.446$ ,  $\ln \bar{N}_2 = 4.148$ , and scatter  $\sigma_{\ln N_{200}|M} = 0.432$  (gray shaded band). The solid and dashed vertical lines indicate the richness ranges of clusters used in the number count and weak lensing constraints, respectively.

Note that we refer to  $\langle \ln N_{200}|M \rangle$  as the mean “richness–mass” relation, as distinct from the mean “mass–richness” relation  $\langle \ln M|N_{200} \rangle$ . In the presence of scatter, one cannot trivially convert from one to the other, since there are more low mass halos to scatter to high richness than vice versa. Furthermore, since we assume log–normal rather than Gaussian scatter in richness, the mean richness at a fixed mass  $\langle N_{200}|M \rangle$  is *not* simply  $\exp \langle \ln N_{200}|M \rangle$ . Rozo et al. (2012a) discussed these issues in the more general context of cluster observables. Finally, we caution that when integrating over a bin in richness, the mean  $\ln M$  is not simply the value of  $\langle \ln M|N_{200} \rangle$  evaluated at the bin center (e.g., compare centers of distributions of the same color in the top and bottom panels of Fig. 2, which we will discuss more later). These effects account for the difference between the mean mass–richness relation quoted by Rozo et al. (2009), which is directly the inferred mean mass of clusters in specified bins of richness, and the richness–mass relation of R10, which is a central power–law derived from a full cosmological fit and more closely analogous to what we do here.

To account for residual uncertainties in the photometric redshift distribution used in the weak lensing analysis, we divide the predicted  $\Delta\Sigma(R)$  by a nuisance parameter  $\beta$  before comparing with the data, so that we are effectively modeling the underlying tangential shear profiles while using  $\beta$  to characterize the multiplicative bias in the conversion to  $\Delta\Sigma(R)$ . We adopt a Gaussian prior with central value  $\beta = 1.0$  and width  $\delta\beta = 0.06$ , somewhat larger than the uncertainty of 0.04 estimated by Rozo et al. (2009). We comment more on the constraints on  $\beta$  in § 5.4 and the prior on  $\beta$  in § 6.

We thus have seven parameters in the model that we fit to the cluster abundance and large scale  $\Delta\Sigma(R)$  data: two cosmological parameters ( $\Omega_m, \sigma_8$ ) that we are hoping to constrain, and five nuisance parameters, among which are ( $\ln \bar{N}_1, \ln \bar{N}_2, \sigma_{\ln N_{200}|M}$ ) of the richness–mass relation,  $\beta$  as the residual bias of the weak lensing shape measurement (hereafter referred to as the “weak lensing bias”), and  $\Delta n_s$  for the modulation of the  $P(k)$  shape.

#### 3.2 Likelihood

We model the number counts and weak lensing measurements for clusters in different bins of richness. Aiming for better statistical rather than extra tomographic constraints, we do not divide our sample into multiple redshift bins, but only retain the whole photometric redshift range as a single bin ( $0.1 < z_{\text{photo}} < 0.3$ ). The observable vector in our likelihood model thus has three components:

1.  $N_i$ : number of clusters in each richness bin  $i$  for  $i \in \{1 \dots 9\}$ .
2.  $\Delta\Sigma_j(R_k)$ : stacked  $\Delta\Sigma$  profile of richness bin  $j$  measured at radius  $R_k$ , for  $j \in \{1 \dots 5\}$  and  $k \in \{1 \dots 6\}$ .
3. Number of clusters with  $N_{200} > 120$ .

We model the combinatorial vector of the 1st and the 2nd components as a multivariate Gaussian (39 variables in total), which is fully specified by its mean vector and covariance matrix. Fig. 1 illustrates the observations of  $N_i$  (gray/red histograms in the left panel) and  $\Delta\Sigma_j(R_k)$  (solid circles in the middle panel) used in our analysis. The richness bins we employed for cluster abundance and weak lensing measurements are listed in Table 1 and 2, respectively. We adopt the same richness bins that R10 used for number counts  $N_i$  and weak lensing profiles  $\Delta\Sigma_j$ ; note that the  $i$  and  $j$  bins are overlapping but not identical, as larger bins are required to achieve reasonable S/N in  $\Delta\Sigma(R)$ . We only use the  $\Delta\Sigma$  measurements at large scales ( $R_k > 5h^{-1}\text{Mpc}$ ). We comment on the choice of cutoff radius at  $R_{\min} = 5h^{-1}\text{Mpc}$  in § 4.2.

For  $N_{200} > 120$ , the assumption of Gaussian fluctuations in number counts is invalid due to the rarity of extreme clusters. Following R10, we model the count of  $N_{200} > 120$  clusters as a Poisson binomial distribution, which is a sum of independent Bernoulli distributions at each integer  $N_{200} > 120$ . The likelihood associated with this tail population of clusters  $\mathcal{L}_{\text{tail}}$  is given in equation 3 of Rozo et al. (2010)<sup>2</sup>.

The final likelihood  $\mathcal{L}$  is then simply the product of the Gaussian likelihood and the Poisson binomial likelihood.

### 3.2.1 Expectation Values

For any given cosmology, the mass function  $dn/dM$  and the  $\Delta\Sigma(R)$  of DM halos can be theoretically predicted as functions of mass  $M$  at each redshift  $z$ . To convert to the total number  $N$  and the average  $\Delta\Sigma(R)$  of clusters with richness  $N_{200}$  and photometric redshift  $z_{\text{photo}}$ , we need to convolve with a kernel that relates the observables ( $N_{200}$  and  $z_{\text{photo}}$ ) to the intrinsic properties ( $M$  and  $z$ ). For our purpose, the kernel function  $\omega_l(M, z)$  is defined as the *expected* differential number of clusters with mass  $M$  at redshift  $z$  that fall into richness bin  $l$  and within our photometric redshift range,

$$\omega_l(M, z) = \frac{\langle dN_l | M, z \rangle}{dM dz}, \quad l \in \{i, j\}. \quad (4)$$

(we use  $i$  for number counts,  $j$  for  $\Delta\Sigma$  bins, and  $l$  generic.) The derivation of  $\omega_l(M, z)$  is similar to that in Rozo et al. (2007b, 2010), and we briefly describe the procedures below.

We start by defining the richness selection function  $\psi_l(N_{200})$ , which is the probability for a cluster of  $N_{200}$  to be selected into the  $l$ -th richness bin. For the richness bins defined by Table 1 and 2,  $\psi_l(N_{200})$  is simply a top-hat bracketed by two ends of the  $l$ -th richness bin. For our calculation, however, we need  $\langle \psi_l | M \rangle$ , the *expected* probability for a cluster of true mass  $M$  to be selected into the  $l$ -th richness bin. Without loss of generality, we drop the subscript  $l$  of  $\psi$  so that

$$\langle \psi | M \rangle = \int dN_{200} P(N_{200} | M) \psi(N_{200}), \quad (5)$$

where  $P(N_{200} | M)$  is the probability of a halo of mass  $M$  observed with richness  $N_{200}$ , specified by the richness–mass relation. The

bottom panel of Fig. 2 shows the  $\langle \psi | M \rangle$  for five richness bins used for the  $\Delta\Sigma(R)$  measurements, given our best-fit model. To a first approximation, these distributions are Gaussian in  $\ln M$ , centered on the value of  $M$  that corresponds to the mean mass–richness relation at the central richness of the bin.

We also consider the photometric redshift selection function  $\phi(z_{\text{photo}})$ , which is defined as the probability for a cluster of measured  $z_{\text{photo}}$  to be selected into the catalog, i.e., a top-hat bracketed by the redshift extent of the catalog. Similarly, we instead need the *expected* spectroscopic redshift selection function for a cluster at spectroscopic redshift  $z$  to appear in the catalog

$$\langle \phi | z \rangle = \int dz_{\text{photo}} P(z_{\text{photo}} | z) \phi(z_{\text{photo}}), \quad (6)$$

where  $P(z_{\text{photo}} | z)$  is the probability for a cluster at true redshift  $z$  to be estimated with photometric redshift  $z_{\text{photo}}$ . This probability is assumed to be Gaussian, centered on spectroscopic redshift  $z$ , with  $\sigma(z_{\text{photo}} | z) = 0.008$  (Koester et al. 2007).

The product of  $\langle \psi | M \rangle$  and  $\langle \phi | z \rangle$  then gives the joint selection probability for a cluster with mass  $M$  at redshift  $z$  to be selected into a given richness bin with  $0.1 < z_{\text{photo}} < 0.3$ . To predict number density weighted averages for cluster properties in the bin, we also need the differential number of clusters with mass  $M$  at redshift  $z$ , which is simply the product of the halo mass function  $dn/dM$  and the differential co-moving volume element  $dV/dz$ . The final kernel function  $\omega(M, z)$  is then obtained via equation (4)

$$\omega(M, z) = \frac{dn}{dM} \frac{dV}{dz} \langle \phi | z \rangle \langle \psi | M \rangle, \quad (7)$$

the integration of which gives the expectation value for the number counts  $N_i$  and  $N_j$

$$\langle N_l \rangle = \int dM dz \omega_l(M, z), \quad l \in \{i, j\}. \quad (8)$$

The top panel in Fig. 2 shows  $\langle dN/d \log M \rangle$ , the distribution of halos within richness bins, which is simply the integration of  $\omega(M, z)$  over redshift, using our best-fit model parameters. Here we clearly see the impact of scatter and mass function slope discussed in § 3.1: the average richness of clusters in a bin of mass is offset from the value of the mean relation evaluated at the center of the mass bin. For example, a  $10^{15} h^{-1} M_{\odot}$  cluster would have a high probability ( $\sim 40\%$ ) of being assigned to the  $N_{200} \in [40 - 70]$  richness bin (orange-colored distributions), but because  $10^{15} h^{-1} M_{\odot}$  clusters are much rarer than lower mass clusters, the number of them represented in this bin is negligibly small. Conversely, the average mass in a bin of richness is offset from the center of  $\langle \psi | M \rangle$  for that bin — the average mass of clusters with  $N_{200} \in [40 - 70]$  is  $\simeq 5 \times 10^{14} h^{-1} M_{\odot}$  (solid orange circle), and as mentioned in § 3.1, the quantity  $\exp \langle \ln M | N_{200} \rangle$  is even more offset from the center of  $\langle \psi | M \rangle$ , landing at  $M \simeq 4.3 \times 10^{14} h^{-1} M_{\odot}$  (vertical orange arrow).

The expectation value for  $\Delta\Sigma_j$  is

$$\langle \Delta\Sigma_j \rangle = \frac{1}{\langle N_j \rangle} \int dM dz \omega_j(M, z) \Delta\Sigma(R | M, z), \quad (9)$$

where  $\Delta\Sigma(R | M, z)$  is the  $\Delta\Sigma(R)$  of halos with mass  $M$  at redshift  $z$ .

For  $\Delta\Sigma(R | M, z)$ , by definition (Miralda-Escude 1991; Sheldon et al. 2004),

$$\Delta\Sigma(R | M, z) \equiv \bar{\Sigma}(< R | M, z) - \bar{\Sigma}(R | M, z), \quad (10)$$

<sup>2</sup> Note they have a typo in equation 3 where the order of the two rhs terms should be reversed

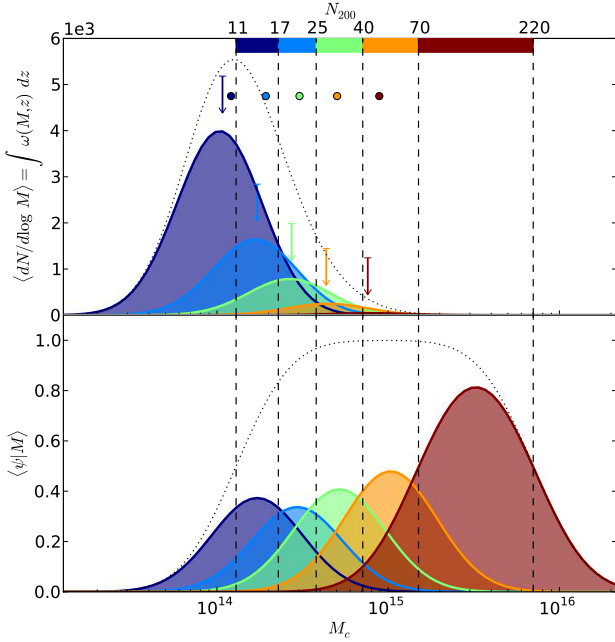


**Figure 2.** Cluster selection for the five richness bins listed in Table 2. *Top:* Distribution of halo masses within each richness bin  $\langle dN/d\log M \rangle$ , as computed from our best-fit model. The dotted curve gives the total number distribution of halos within the five bins. Solid circles and vertical arrows indicate the values of  $\langle M|N_{200} \rangle$  and  $\exp(\ln M|N_{200})$ , respectively, for each richness bin. *Bottom:* Richness selection function  $\langle \psi|M \rangle$ . Each curve shows the probability of halos being assigned to each richness bin at mass  $M_c$ , as computed from our best-fit  $P(N_{200}|M)$ . Dotted curve is the sum of the five curves, giving the probability of halos being included in the  $\Delta\Sigma(R)$  measurements. In each panel, each color represents one of the five richness bins. The top x-axis indicates the mean richness that corresponds to the mass at the bottom x-axis, given by our best-fit mean richness–mass relation. Vertical dashed lines show the demarcation of richness bins based on the top x-axis.

where

$$\bar{\Sigma}(< R|M, z) = \int_0^R dr_p r_p \int_{-\infty}^{+\infty} dr_z \xi_{\text{hm}}(\sqrt{r_p^2 + r_z^2}, M) \times \rho_{\text{m},z} \frac{2}{R^2} \quad (11)$$

and

$$\bar{\Sigma}(R|M, z) = \rho_{\text{m},z} \int_{-\infty}^{+\infty} \xi_{\text{hm}}(\sqrt{R^2 + r_z^2}, M) dr_z. \quad (12)$$

In the above equations,  $\rho_{\text{m},z} = \Omega_{\text{m}} \rho_{\text{c},0} (1+z)^3$  is the mean density of the universe at  $z$ , and  $\xi_{\text{hm}}(r, M)$  is the halo-matter cross-correlation function at 3-D distance  $r$  for halos with mass  $M$ .

For  $\xi_{\text{hm}}(r, M)$ , we use a variant of the model proposed by HW08

$$\xi_{\text{hm}}(r, M) = \begin{cases} \xi_{1\text{h}} & \text{if } \xi_{1\text{h}} \geq \xi_{2\text{h}}, \\ \xi_{2\text{h}} & \text{if } \xi_{1\text{h}} < \xi_{2\text{h}}, \end{cases} \quad \xi_{1\text{h}} = \frac{\rho_{\text{halo}}(r, M)}{\rho_{\text{m}}} - 1, \quad \xi_{2\text{h}} = b(M) \xi_{\text{nl}}. \quad (13)$$

Here  $\xi_{1\text{h}}$  and  $\xi_{2\text{h}}$  are the so-called “1-halo” and “2-halo” terms in the halo model (see Cooray & Sheth 2002 for a review),  $\rho_{\text{halo}}(r, M)$  is the NFW density profile of halos with mass  $M$ , and

$b(M)$  is the halo bias function. The difference from the original HW08 prescription is that we use the non-linear matter autocorrelation  $\xi_{\text{nl}}$  computed from the fitting formula of Smith et al. (2003) instead of the linear prediction  $\xi_{\text{lin}}$ . We demonstrate that this modification provides an accurate approximation of large scale measurement of  $\Delta\Sigma(R|M, z)$  from N-body simulations in § 4.2.

### 3.2.2 Covariance Matrix

The covariance matrix of the model  $C$  is comprised of three sub-blocks,  $C_{\text{NN}}$  (abundance–abundance),  $C_{\text{N}\Sigma}$  (abundance–shear), and  $C_{\Sigma\Sigma}$  (shear–shear). We begin with  $C_{\text{NN}}$ , which has two independent sources of uncertainties:

- Sample variance due to limited survey volume (a.k.a. cosmic variance).
- Poisson fluctuations in cluster number counting (a.k.a. shot noise).

Thus the covariance between cluster number counts in two richness bins  $i$  and  $i'$  is the sum of two components

$$C_{\text{N}^i \text{N}^{i'}} = C_{\text{N}^i \text{N}^{i'}}^{\text{sample}} + C_{\text{N}^i \text{N}^{i'}}^{\text{Poisson}}, \quad (14)$$

and, as will become apparent below, the diagonal parts of both components scale with survey volume in a similar fashion. We will describe each in turn.

Assuming the clustering bias  $b$  of clusters is linear with respect to the underlying density fluctuation on the scale of the survey  $R_V$ , the sample variance term is simply (Hu & Kravtsov 2003)

$$C_{\text{N}^i \text{N}^{i'}}^{\text{sample}} = \langle N_i \rangle \langle N_{i'} \rangle \langle b_i \rangle \langle b_{i'} \rangle \sigma^2(R_V), \quad (15)$$

where

$$\langle b_l \rangle = \frac{1}{\langle N_{i,i'} \rangle} \int dM dz b(M) \omega_l(M, z), \quad l \in \{i, i'\}, \quad (16)$$

and  $\sigma^2(R_V)$  is the variance of the linear density fluctuation field on scale  $R_V$ , which we assumed to be adequately approximated by the radius of a sphere that has the same volume as the survey. On relevant scales,  $\sigma^2(R)$  is approximately proportional to  $1/V$ , so the diagonal terms  $C_{\text{N}^i \text{N}^i}^{\text{sample}} \propto \langle N_i^2 \rangle / V \propto V$  (Hu & Kravtsov 2003).

The Poisson fluctuation term is trivial,

$$C_{\text{N}^i \text{N}^{i'}}^{\text{Poisson}} = \delta_{ii'} \langle N_i \rangle, \quad (17)$$

i.e., it is diagonal and the variance is equal to the expectation value of the number counts in each richness bin. Our covariance matrix differs from that of R10 in that we do not include the “stochasticity” contribution in R10. One might think that scatter between richness and mass would introduce off-diagonal covariances because clusters that scatter out of one richness bin will scatter into a neighboring bin. Indeed, when the total number of halos is held fixed, such covariance do occur. However, when one simultaneously considers both Poisson sampling and the stochasticity due to scatter in the richness–mass relation, one finds that the two are coupled in such a way that the naive Poisson terms represent the full covariance matrix. We have explicitly verified this via numerical experiments. Simply adding the Poisson and “stochastic” covariance matrices, as was done in R10, is incorrect, and the naive Poisson term alone captures the full variance due to Poisson fluctuations and the stochasticity of the richness–mass relation.

Fig. 3 compares the two components of  $C_{\text{N}^i \text{N}^{i'}}$  as computed for our best-fit model. The diagonal elements of the sample variance component are much weaker than the Poisson errors



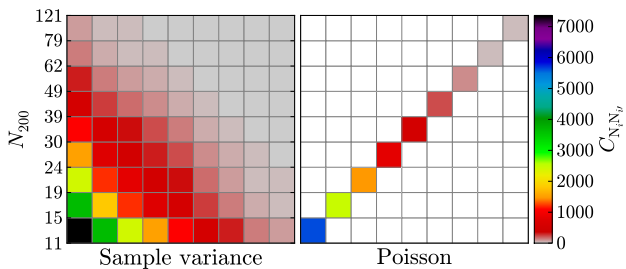


**Figure 3.** Comparison between the two components of  $C_{N_i N_{i'}}$ :  $C_{N_i N_{i'}}^{\text{sample}}$  (left) and  $C_{N_i N_{i'}}^{\text{Poisson}}$  (right), as computed for the best-fit model. Each panel is a  $9 \times 9$  matrix color-coded by the value of  $C_{N_i N_{i'}}$ . The richness bins are shown on the y-axis of the left panel.

except for the lowest richness bin, where sample variance dominates (Hu & Kravtsov 2003). Sample variance also produces positive off-diagonal terms. Overall, the off-diagonal terms are smaller than diagonal terms, but not completely negligible.

The other two sub-blocks,  $C_{N\Sigma}$  and  $C_{\Sigma\Sigma}$ , also have contributions from sample variance in the cluster-mass correlation function. However, the dominant contributions to the  $\Delta\Sigma(R)$  errors come from statistical errors in the weak lensing measurements themselves. One major contribution to these errors is shape noise from the random orientations of source galaxies; with rms galaxy ellipticity  $\sim 0.3$ , one needs  $N \sim (0.3/\gamma)^2$  sources to measure a shear  $\gamma$  at  $S/N = 1$ , and with the surface density  $n_{\text{eff}} \sim 1 \text{ arcmin}^{-2}$  typical of SDSS weak lensing data, the  $S/N \ll 1$  for any individual clusters. (Tangential shear is roughly  $\gamma_T \sim 0.01$  near the cluster virial radius and smaller beyond.) A second contribution comes from coherent cosmic shear lensing of source galaxies by foreground or background structure not associated with the lensing cluster (Dodelson 2004; Hoekstra et al. 2011). For the  $\Delta\Sigma(R)$  covariance matrix in each richness bin, we use the empirical estimates of S09 based on jackknife re-sampling of the data set in large area patches, where the measurement regions around clusters do not overlap, shape noise errors should be diagonal and drop with the square root of the number of source galaxies in each radial bin. However, as mentioned in S09, the jackknife errors at  $R > 5h^{-1}\text{Mpc}$  become substantially larger than this naive expectation, and there are significant off-diagonal terms for different radial bins. These large, correlated errors presumably reflect the coherent cosmic shear effect described above, though they could also be affected by spatially coherent fluctuations in the quality of point spread function (PSF) correlation. In principle there is also a  $C_{N\Sigma}$  sub-block to the covariance matrix, but we ignore it here because the  $\Delta\Sigma(R)$  errors are dominated by measurement error not sample variance.

Additionally, the entire covariance matrix is affected by uncertainties in the completeness and the purity of the MaxBCG cluster sample. Interlopers and missing clusters can both bias the number counts, though the two effects tend to cancel. For  $\Delta\Sigma(R)$ , missing clusters only increase errors, while interlopers can bias the measurement via dilution. The magnitude of this effect is difficult to estimate without detailed simulations, since the main source of “interlopers” will be random superpositions of smaller clusters at different redshifts, and the weak lensing signal from the superposed systems may be similar to that expected from a single system of the estimated richness (in which case there is no dilution). For  $N_{200} > 11$ , the purity and completeness of the MaxBCG catalog is estimated to be at the  $\sim 95\%$  level or higher, so any associated

**Table 3.** Prior Specifications. The  $P(k)$  shape is generated from the best-fit cosmological parameters from Reid10, and  $\sigma_{\ln M|N_{200}}$  is not a model parameter but an observable. Priors that contain the form  $[a, b]$  mean the parameter in question is restricted to values within that range. Priors that contain the form  $x = a \pm \delta a$  refer to a Gaussian prior of mean  $\langle x \rangle = a$  and variance  $\text{Var}(x) = (\delta a)^2$ . The combination of the two forms is a Truncated Gaussian. Uninformative priors mean the parameter in question is absolutely unrestricted.

Parameter	Prior
$\Omega_m$	Uniform on [0.05, 0.95]
$\sigma_8$	Uniform on [0.40, 1.20]
$\sigma_{\ln N_{200} M}$	Uniform on [0.10, 1.50]
$\beta$	Truncated Gaussian $1.00 \pm 0.06$ on [0.50, 1.50]
$\ln \bar{N}_1$	Uninformative
$\ln \bar{N}_2$	Uninformative
$\Delta n_s$	Truncated Gaussian $0.000 \pm 0.013$ on [-0.1, +0.1]
$P(k)$ shape	“ $\Lambda$ CDM” Column of table 3 in Reid et al. (2010)
$\sigma_{\ln M N_{200}}$	Gaussian $0.45 \pm 0.10$ ; Rozo et al. (2009)

biases should be small, though they can be coherent across richness and radial bins. Following R10, we define the magnitude of this bias to be  $\lambda \simeq 1 \pm 0.05$  and add  $\text{Var}(\lambda) = 0.05^2$  to the fractional errors in all elements of  $C_{NN}$  and diagonal elements of  $C_{\Sigma\Sigma}$ , respectively. We comment on our treatments for  $\lambda$  in § 6.

### 3.3 Priors

Table 3 summarizes the priors assumed in our analysis. To ensure that our results are driven by the data, we place either uniform or unrestrictive priors on five of our seven model parameters,  $\Omega_m$ ,  $\sigma_8$ ,  $\sigma_{\ln N_{200}|M}$ ,  $\ln \bar{N}_1$ , and  $\ln \bar{N}_2$ , and conservative truncated Gaussian priors on the other two,  $\beta$  and  $\Delta n_s$ . We take the  $P(k)$  shape to be that of the best-fit  $\Lambda$ CDM model from Reid10, multiplied by  $(k/1 h\text{Mpc}^{-1})^{\Delta n_s}$  to allow minor modulation.<sup>3</sup> Note that while this is a “ $\Lambda$ CDM” power spectrum for specific cosmological parameters, we are treating it here as the empirical description of the observed shape of the galaxy power spectrum. We also place priors on  $\sigma_{\ln M|N_{200}}$ , the converse scatter defined as the dispersion in log-mass in the fixed richness bin  $N_{200}=[38, 42]$ . Following R10, we take the prior on  $\sigma_{\ln M|N_{200}}$  directly from the analysis in Rozo et al. (2009),  $\sigma_{\ln M|N_{200}} = 0.45 \pm 0.10$ , which is derived by requiring consistency among the MaxBCG  $L_X$ - $N_{200}$  relation, the MaxBCG richness-mass relation from weak lensing, and the  $L_X$ - $M$  relation measured in the 400d survey (Burenin et al. 2007) by Vikhlinin et al. (2009), as well as the scatters within each of the three scaling relationships.

## 4 TESTS USING SIMULATIONS AND MOCK DATA SETS

### 4.1 Basic Implementation

For the linear matter power spectrum in our likelihood calculation, we take the cosmological parameters inferred by Reid10 and compute  $P_{\text{lin}}(k)$  using the low-baryon transfer function of Eisenstein & Hu (1999), which is a good approximation to the

<sup>3</sup> The choice of pivotal wavenumber is arbitrary as it does not affect the  $P(k)$  shape.

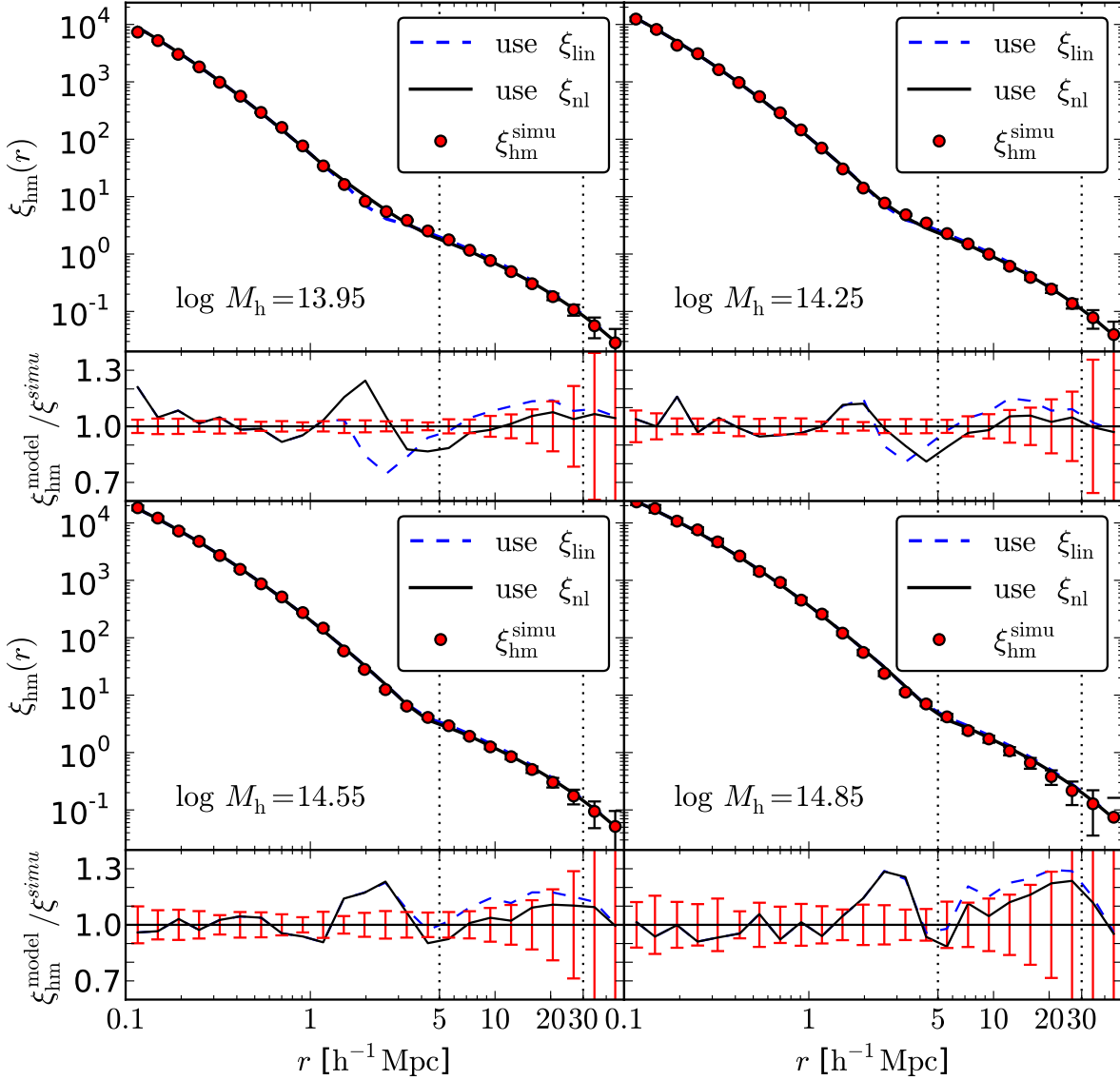


**Figure 4.** Comparison between the 3D halo–matter cross–correlation profiles predicted by the original HW08 prescription (dashed lines), predicted by our modified prescription that uses the non-linear correlation function (solid lines), and measured from simulation (solid circles with errorbars), for four different halo masses at  $z = 0$ . For each mass, the lower subpanel shows the ratios between model predictions and simulation measurement. Errorbars on the simulation measurement in the upper panels are estimated from jackknife sub-sampling of the simulation box and propagated to the ratio curves. Our analysis in this paper uses measurements of  $\Delta\Sigma(R)$  beyond a projected co-moving separation of  $5h^{-1}\text{Mpc}$ , marked by the vertical dotted lines.

full transfer function on scales well below the BAO scale. We refer to this linear power spectrum as  $P_{\text{Reid10}}(k)$ , as it fits their power spectrum measurements of SDSS galaxies by construction. To compute the non-linear matter correlation function  $\xi_{\text{nl}}$ , we use the prescription from Smith et al. (2003) to generate  $P_{\text{nl}}(k)$  for Fourier transforming to  $\xi_{\text{nl}}$ . The halo mass function and the halo bias function are from Tinker et al. (2008) and Tinker et al. (2010), respectively, with the halo mass defined by  $M \equiv M_{200m} = 200\rho_m V_{\text{sphere}}(r_{200m})$ . We use the NFW (Navarro et al. 1996) halo density profile for  $\rho_{\text{halo}}(r, M)$ . The halo mass–concentration relationship is from the fitting formula of Zhao et al. (2009), which accurately recovers the flattening of halo concentration at high masses. (In MaxBCG we do not expect an upturn, which only shows up at redshifts beyond 1; see Prada et al. 2012). In the parameter inference stage, the posterior distribution is derived us-

ing a Markov Chain Monte Carlo (MCMC), where an Adaptive Metropolis step method is utilized during the burn-in period to expedite the exploration of highly correlated parameter space. For each MCMC chain, we perform 320,000 iterations, 20,000 of which belong to the burn-in period for adaptively tuning the steps. To eliminate the tiny amount of residual correlation between adjacent iterations, we further thin the chain by a factor of 10 to obtain our final results.

## 4.2 Halo-Mass Correlation Function

To extract maximum cosmological information from the S09  $\Delta\Sigma(R)$  measurements, one should simultaneously fit the data on all scales. However, as already discussed in the introduction, we have elected to focus on large scales in this paper so that our



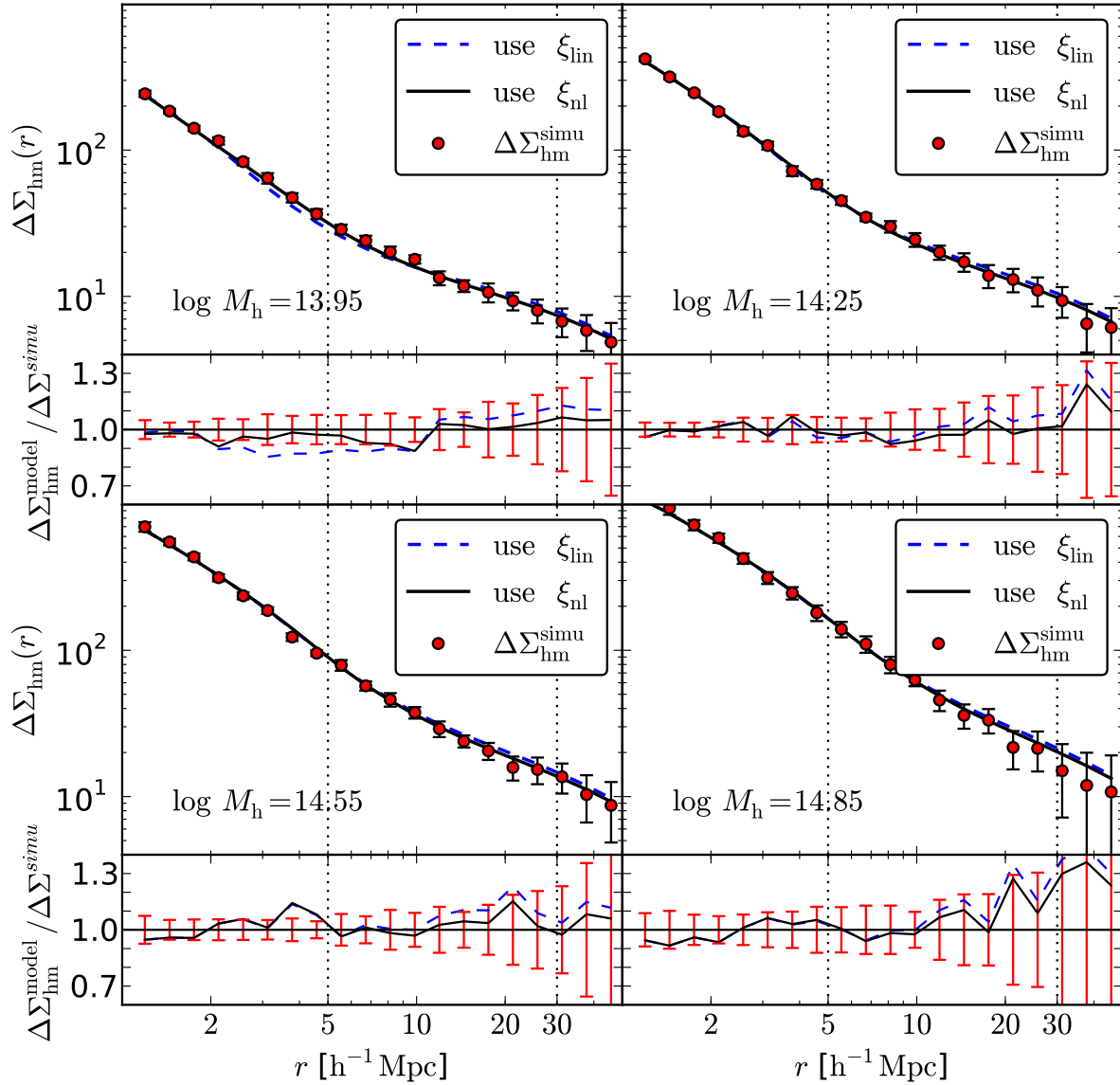


**Figure 5.** Similar to Fig. 4 but for the 2D halo surface density contrast profiles.

constraints are complementary to those derived for the MaxBCG sample by R10, who measured the cluster mass function using a richness–mass relation calibrated by the S09 data on small scales. Restricting our analysis to large scales also allows us to avoid two sources of systematic error, one observational and one theoretical. The observational systematic is the effect of cluster mis-centering, which tends to depress  $\Delta\Sigma(R)$  at small scales. This effect can be estimated from detailed simulations, but with some uncertainties associated with the baryonic physics (Sanderson et al. 2009) and the optical cluster finder (Johnston et al. 2007). The theoretical systematic is the uncertainty in the halo–mass correlation function in the transitional region between the NFW halo mass profile and the large-scale regime where it is a linearly biased multiple of the matter correlation function. We choose our minimum scale  $R_{\min}$  so that this theoretical systematic is small compared to the observational uncertainties of the S09 measurements.

To determine the cutoff scale  $R_{\min}$ , and to test the accuracy of our model of  $\Delta\Sigma(R)$  beyond  $R_{\min}$ , we use halos in cosmo-

logical simulations. The simulation we use is the “L1000W” presented in Tinker et al. (2008, 2010), where the halo mass function and bias function are calibrated. It evolves  $1024^3$  particles with  $m_p = 6.98 \times 10^{10} h^{-1} M_\odot$  in a periodic box of co-moving length  $1000 h^{-1} \text{Mpc}$  using the Adaptive Refinement Tree (ART; Kravtsov et al. 1997; Gottloeber & Klypin 2008) code. For the mass scales we consider here,  $M > 5 \times 10^{13} h^{-1} M_\odot$ , it has at least  $\sim 1000$  particles for each halo and is thus well-suited for the study of  $\xi_{\text{hm}}$  and  $\Delta\Sigma$ . For the model of  $\xi_{\text{hm}}$ , we adapt the original HW08 prescription by using  $\xi_{\text{nl}}(r)$  as in equation (13), so that  $\xi_{\text{hm}}$  is more accurate on large scales. There are other formulas for  $\xi_{\text{hm}}$  in the literature, but it is not clear whether any formulation applies universally across cosmologies. The large scale behavior should be dictated by linear theory in any case, and the HW08 model appears adequate for our present application.

Fig. 4 compares different  $\xi_{\text{hm}}$  profiles predicted by the original HW08 prescription (dashed lines), predicted by our modified prescription (solid lines), and measured from simulation (solid cir-

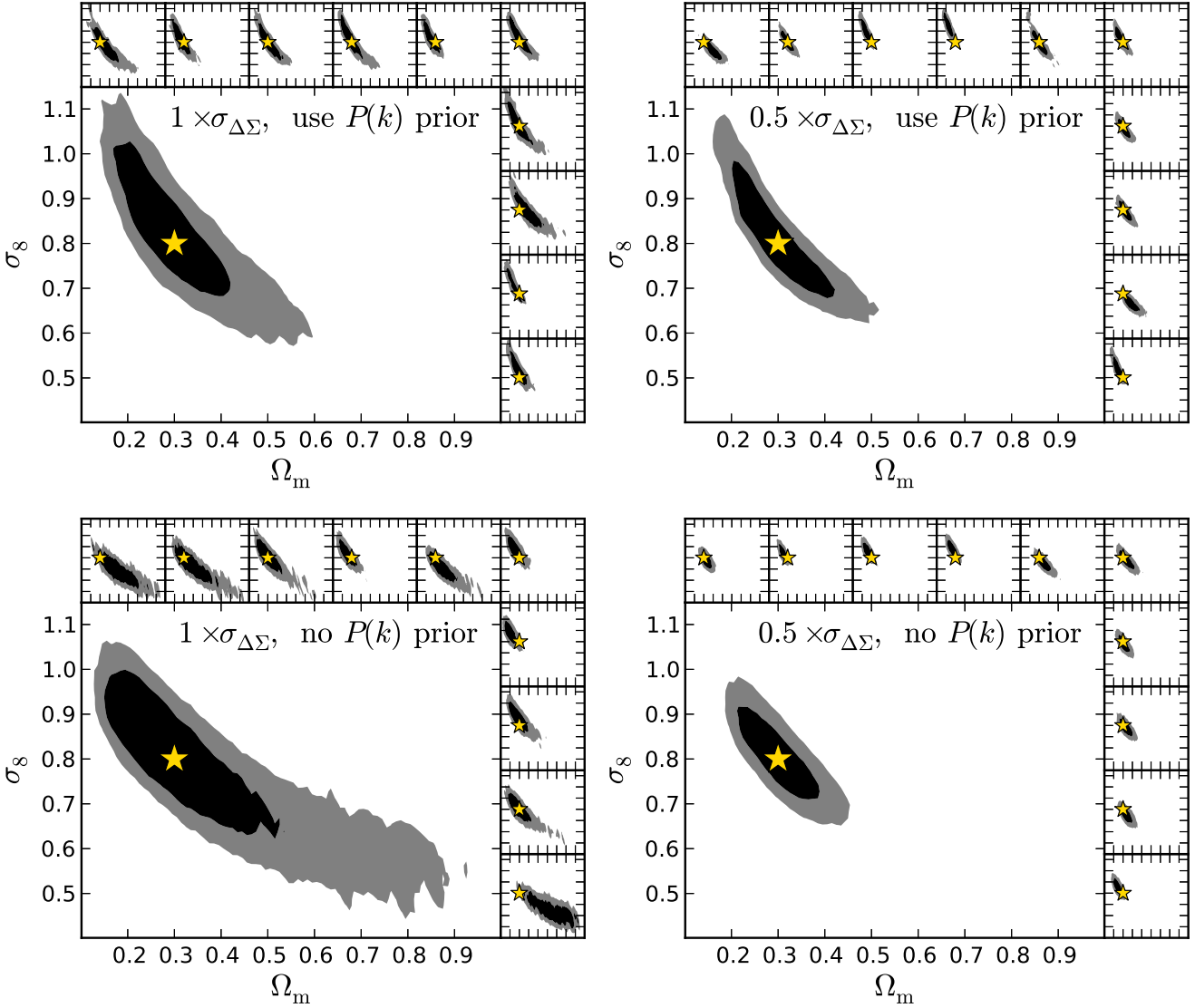


**Figure 6.** The effect of the  $P(k)$  shape prior on the  $\Omega_m$ – $\sigma_8$  constraint using mock data. The two left panels compare the confidence regions derived with (top) and without (bottom) using the  $P(k)$  shape prior for the mock data with the original jackknife errors. The two right panels show a similar comparison for the mock data with weak-lensing errors shrunk by  $1/2$ . In each panel, the contours in the embedded sub-panels are the confidence regions for the 10 individual realizations, and the contours in the main panel are the results after combining all 10 MCMC chains. Each set of contours shows 95% and 68% confidence regions inwards, and the star on top indicates the input cosmology ( $\Omega_m=0.30$ ,  $\sigma_8=0.80$ ) for generating the mock data. For the “no  $P(k)$  prior” cases, we compute the linear power spectrum explicitly for each iteration in the MCMC chains.

cles) at  $z = 0$ , for four halo masses that span the relevant mass range of our cluster sample. The errorbars are from jackknife re-sampling of octants of the simulation box. Both the original and the modified models recover  $\xi_{\text{hm}}$  on small scales ( $< 1h^{-1}\text{Mpc}$ ) very well (within 10%) because of the success of the NFW profile in describing halo density profiles within  $r_{\text{vir}}$ . On the transitional scales between  $1h^{-1}\text{Mpc}$  and  $5h^{-1}\text{Mpc}$ , both models show discrepancies with the simulation of up to 20 – 30% due to the discontinuous change of the prescription between the 1-halo and 2-halo regimes. Beyond  $5h^{-1}\text{Mpc}$ , the modified model clearly outperforms the original one, agreeing with the simulation within the errorbars in all mass bins, and agreeing to within 10% except for the highest mass bin, where the measurement error is large due to the small number of very massive clusters in the simulation. (In

detail, the  $6h^{-1}\text{Mpc}$  prediction is outside the error bar in the two lowest mass bins.)

Fig. 5 shows the same comparison between the two models and the simulation measurement for  $\Delta\Sigma(R)$ , the quantity we care most about. Similar to the  $\xi_{\text{hm}}$  case, the models agree with the simulation to within a few per cent below  $\sim 2h^{-1}\text{Mpc}$ , and for most of the transitional scales between  $2h^{-1}\text{Mpc}$  and  $5h^{-1}\text{Mpc}$ ; projection dilutes but does not eliminate the effect of the “discontinuity spikes” seen in Fig. 4. Beyond  $5h^{-1}\text{Mpc}$ , the original HW08 model generally has some  $> 15\%$  deviations from the simulation measurement in all mass bins, while the modified model is in excellent agreement with the simulation, to within 5% in the three lowest mass bins and within the measurement uncertainties (30%) in the highest mass bin. Note that the S09  $\Delta\Sigma$  measurement also

has  $\sim 30\%$  uncertainties on large scales. We test the effect of dropping the  $\Delta\Sigma(R)$  measurements for the highest richness bin in § 6.

To bracket the redshift extent of the MaxBCG clusters, we have also done the comparison test using the simulation output at  $z = 0.3$ , and the results are similar. Based on the results of the tests, we conclude that the impact of scale-dependent bias on  $\Delta\Sigma(R)$  is very weak on scales beyond  $5h^{-1}\text{Mpc}$  using the modified HW08 model in Equation 13, well below the uncertainties in the S09 measurements. Therefore, we choose to use the stacked weak lensing observations beyond co-moving scale of  $\sim 6h^{-1}\text{Mpc}$ , which for the redshifts of our cluster sample corresponds to a cutoff radius  $R_{\text{min}}$  of  $5h^{-1}\text{Mpc}$  in physical units.

### 4.3 Power Spectrum Shape as a Prior

Once we have determined  $R_{\text{min}}$ , the large scale 3D density contrast profile of halos,  $\Omega_m \xi_{\text{hm}}(r, M)$ , carries clean and easily accessible cosmological information, as  $\Omega_m \xi_{\text{hm}}(r, M) \propto \Omega_m b(M) \sigma_8^2$  if we know the shape of the matter correlation function  $\xi_{\text{mm}}(r)$  well. However, our measurements of  $\Delta\Sigma(R)$  provide only limited constraints on the shape of  $\xi_{\text{mm}}(r)$ , in part because of projection, in part because we use only large scale measurements, and most of all because the statistical errors in the  $\Delta\Sigma(R)$  measurements remain fairly large. Uncertainty in the  $\xi_{\text{mm}}(r)$  shape would limit our ability to optimally combine measurements from multiple scales, and it would limit our ability to translate our measurements from these scales to a value of  $\sigma_8$ , which is defined at the specific scale of  $8h^{-1}\text{Mpc}$ .

To circumvent this problem, we introduce the shape of the power spectrum measured from SDSS Luminous Red Galaxies by Reid10 as a prior in our Bayesian analysis, without introducing any explicit priors on individual cosmological parameters. We are taking advantage of the fact that the shape of the power spectrum is well constrained observationally by galaxy clustering data, even though it is not well constrained by our  $\Delta\Sigma(R)$  measurements. We allow deviations from  $P_{\text{Reid10}}(k)$  as parameterized by  $\Delta n_s$ . To test the performance of the  $P(k)$  shape as a prior and its sensitivity to uncertainties in  $\Delta\Sigma(R)$ , we generate two sets of mock data, one using the original S09 jackknife errors, and one using half the S09 errors. For each mock set, we produce 10 random realizations from the multivariate Gaussian describing the cluster counts and  $\Delta\Sigma(R)$  values, using the parameters  $\Omega_m = 0.30$ ,  $\sigma_8 = 0.80$ ,  $\sigma_{\ln N_{200|M}} = 0.36$ ,  $\beta = 1.0$ ,  $\ln \bar{N}_1 = 2.4$ ,  $\ln \bar{N}_2 = 4.2$ , and  $\Delta n_s = 0.0$ , along with other cosmological parameters set as the WMAP7 values. We also compute the  $P(k)$  shape from the same cosmology, and we perform MCMC analyses on the 10 random realizations of each mock data set with and without using the  $P(k)$  shape prior. When there is no shape prior used, we fix all the cosmological parameters to be their WMAP7 values except for  $\Omega_m$  and  $\sigma_8$ , and the  $P(k)$  shape varies with  $\Omega_m$  according to the  $\Lambda\text{CDM}$  prediction.

Fig. 6 shows the effect of introducing the  $P(k)$  shape prior on the  $\Omega_m$ – $\sigma_8$  constraints for the two mock data sets. For the mock data with original weak-lensing errors (left two panels), when the  $P(k)$  shape is *a priori* unknown (bottom left panel), the analysis generally accepts an incorrect region of high- $\Omega_m$  and low- $\sigma_8$  within 95% confidence, allowing models in which the associated  $P(k)$  becomes much bluer due to an earlier epoch of matter–radiation equality and transforms into a  $\xi_{\text{mm}}$  that is too strong (weak) on small (large) scales. Despite being physically unlikely, after projection this model leads to  $\Delta\Sigma(R)$  profiles that are consistent with the mock data within the errors. When the shape

**Table 4.** Best-fit Models

Parameter	MaxBCG	MaxBCG+WMAP7
$\Omega_m$	$0.325^{+0.086}_{-0.067}$	$0.298^{+0.019}_{-0.020}$
$\sigma_8$	$0.828^{+0.111}_{-0.097}$	$0.831^{+0.020}_{-0.020}$
$\sigma_{\ln N_{200 M}}$	$0.432^{+0.063}_{-0.068}$	$0.436^{+0.012}_{-0.024}$
$\beta$	$1.004^{+0.060}_{-0.142}$	$0.968^{+0.034}_{-0.030}$
$\ln \bar{N}_1$	$2.446^{+0.127}_{-0.249}$	$2.465^{+0.052}_{-0.129}$
$\ln \bar{N}_2$	$4.148^{+0.229}_{-0.229}$	$4.163^{+0.068}_{-0.068}$
$\Delta n_s$	$0.001^{+0.013}_{-0.013}$	$0.001^{+0.001}_{-0.001}$

prior is used (top left panel), the high- $\Omega_m$  and low- $\sigma_8$  region is correctly rejected by the model, demonstrating the efficacy of the shape prior in eliminating the degeneracy between uncertainties in the  $P(k)$  shape and cosmological parameters.

For the mock data with smaller weak-lensing errors (right two panels), both  $\Omega_m$  and  $\sigma_8$  are well constrained either with or without using the shape prior, showing that the shape degeneracy greatly diminishes with the reduced weak-lensing errors even though we do not use small scale  $\Delta\Sigma(R)$  information. The contours are slightly more elongated when the shape prior is used (top right panel), because it is easier for extreme values of  $\Omega_m$  and  $\sigma_8$  to fit the observed cluster richness function when the right  $P(k)$  shape is directly known compared to when the right  $n_s$ ,  $\Omega_b$ ,  $\Omega_\nu$ , and  $h$  are known. In other words, incorrect values of  $\Omega_m$  now produce deviations in the shape of  $\Delta\Sigma(R)$  that are detectable with the smaller errors. Fig. 6 also demonstrates that the uncertainties of our constraints depend crucially on the statistical errors in the weak lensing measurement on large scales — the  $1\sigma$  uncertainties in  $\Omega_m$  and  $\sigma_8$  are reduced by  $\sim 45\%$  after  $\sigma_{\Delta\Sigma}$  shrinks by a factor of two in the lower right panel.

## 5 PARAMETER CONSTRAINTS

Our best-fit model is summarized in the first column of Table 4, where for each parameter we quote the median (50%) as central value and the [18.54%, 84.16%] interval as  $\pm 1\sigma$  uncertainties.

Before presenting the detailed results of our analysis, it is instructive to illustrate how the addition of large scale weak lensing measurements helps break the degeneracy in cluster abundance measurements among the cosmological parameters  $\Omega_m$  and  $\sigma_8$  and the nuisance parameter  $\sigma_{\ln N_{200|M}}$ . The experiments shown in Fig. 7 are designed to serve this purpose, providing a more detailed form of the approximate argument sketched in the introduction. Starting from the fiducial model (Table 4, column 2) that matches both the cluster number counts and  $\Delta\Sigma(R)$  data, in each row of Fig. 7, we raise one of the three key parameters (from top to bottom:  $\Omega_m$ ,  $\sigma_8$ , and  $\sigma_{\ln N_{200|M}}$ ) by a factor of 1.5 from its fiducial value while keeping the other two parameters fixed at their fiducial values. We then re-fit to the cluster abundance data *alone* by varying the mean richness–mass relation. The new best-fit model in each row thus represents one of three families of false models that are indistinguishable from the underlying true model if we only employ the cluster abundance data for constraint. With the modified richness–mass relation in the right column, the new best-fit model predicts cluster number counts that can match the original data (left column) but different  $\Delta\Sigma(R)$  profiles that cannot (middle column). In detail,

- When  $\Omega_m$  is increased (top row), there is no change in the am-

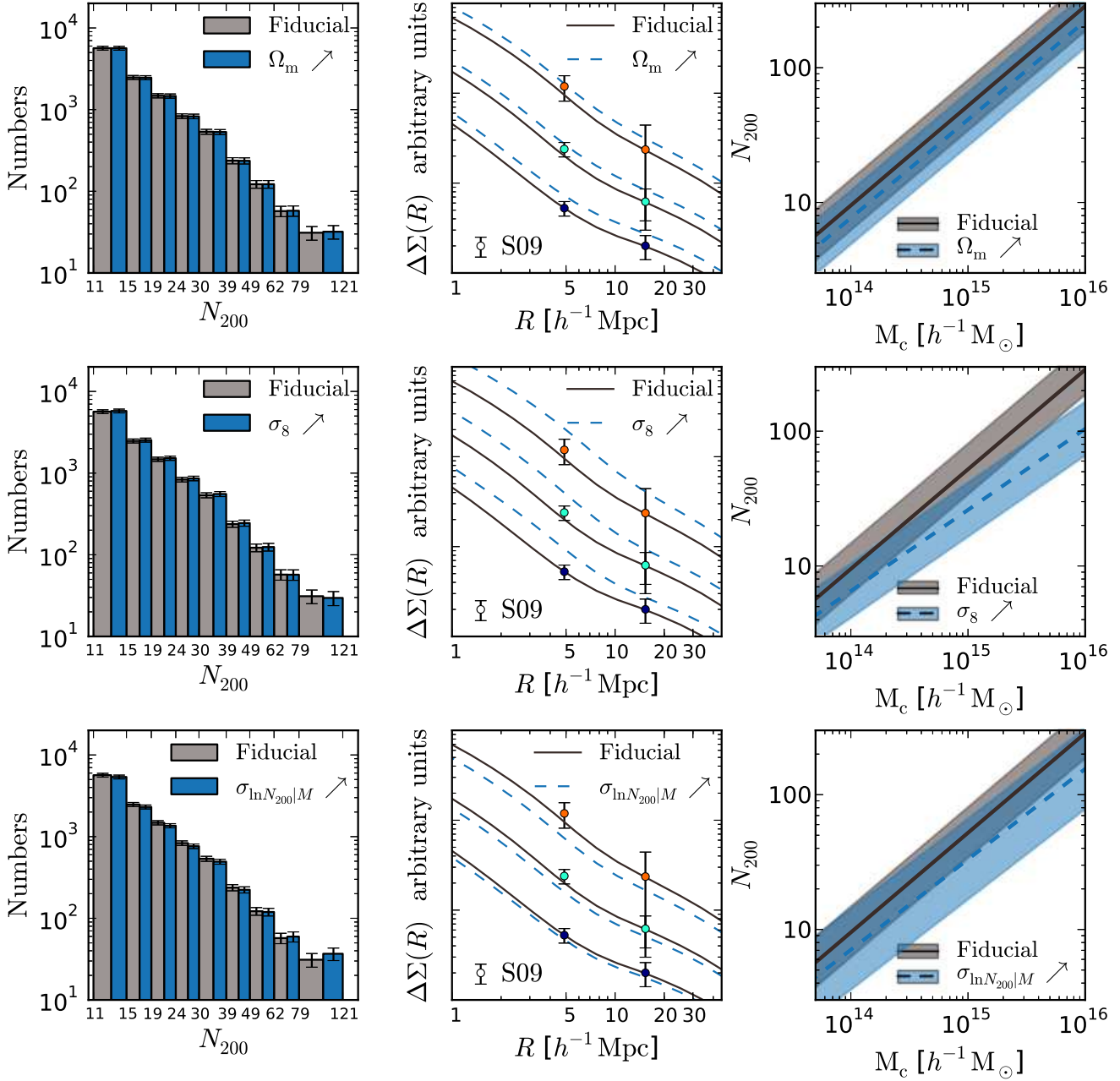


**Figure 7.** Illustration of the underlying methodology of our analysis. In each row, one of the three key parameters (from top to bottom:  $\Omega_m$ ,  $\sigma_8$ , and  $\sigma_{\ln N_{200}|M}$ ) is increased from its fiducial value by a factor of 1.5, and we vary the mean richness–mass relation (blue vs. gray bands in the right column) to find a new best-fit to match the cluster number counts (blue vs. gray histograms in the left column). The panels in the middle column then compare the  $\Delta\Sigma(R)$  profiles predicted by the new best-fit model (blue dashed curves) to the fiducial profiles (gray solid curves). Points with error bars indicate the S09 measurements of  $\Delta\Sigma(R)$  at  $5h^{-1}\text{Mpc}$  and  $15h^{-1}\text{Mpc}$  for the three richness bins. See the text for more details.

plitude of clustering except for an overall change of density, so the halo mass and bias functions both shift uniformly to higher masses. Matching the observed number counts only requires a decrease in the overall amplitude of the mean richness–mass relation. Since there is no change in the cluster bias at fixed richness, the boost in the  $\Delta\Sigma(R)$  profiles is directly caused by the increase in  $\Omega_m$  and is thus independent of distance and richness.

- When  $\sigma_8$  is increased (middle row), the halo mass function changes amplitude and shape: the abundance of halos throughout the cluster mass regime increases, but the increase is larger

at higher masses. To fit the observed abundance as a function of richness, the mean richness–mass relation must tilt downward, becoming shallower than the fiducial relation. This change suffices to reproduce the original number counts, but the  $\Delta\Sigma(R)$  profiles shift upward because of the growth in the amplitude of  $\xi_{\text{mm}}(r)$ . This growth ( $\propto \sigma_8^2$ ) is partly compensated by a reduction in halo bias factors, but this reduction is mass-dependent, with the consequence that  $\Delta\Sigma(R)$  grows more for high richness clusters than for low richness clusters.

- When  $\sigma_{\ln N_{200}|M}$  is increased (bottom row), it has very sim-

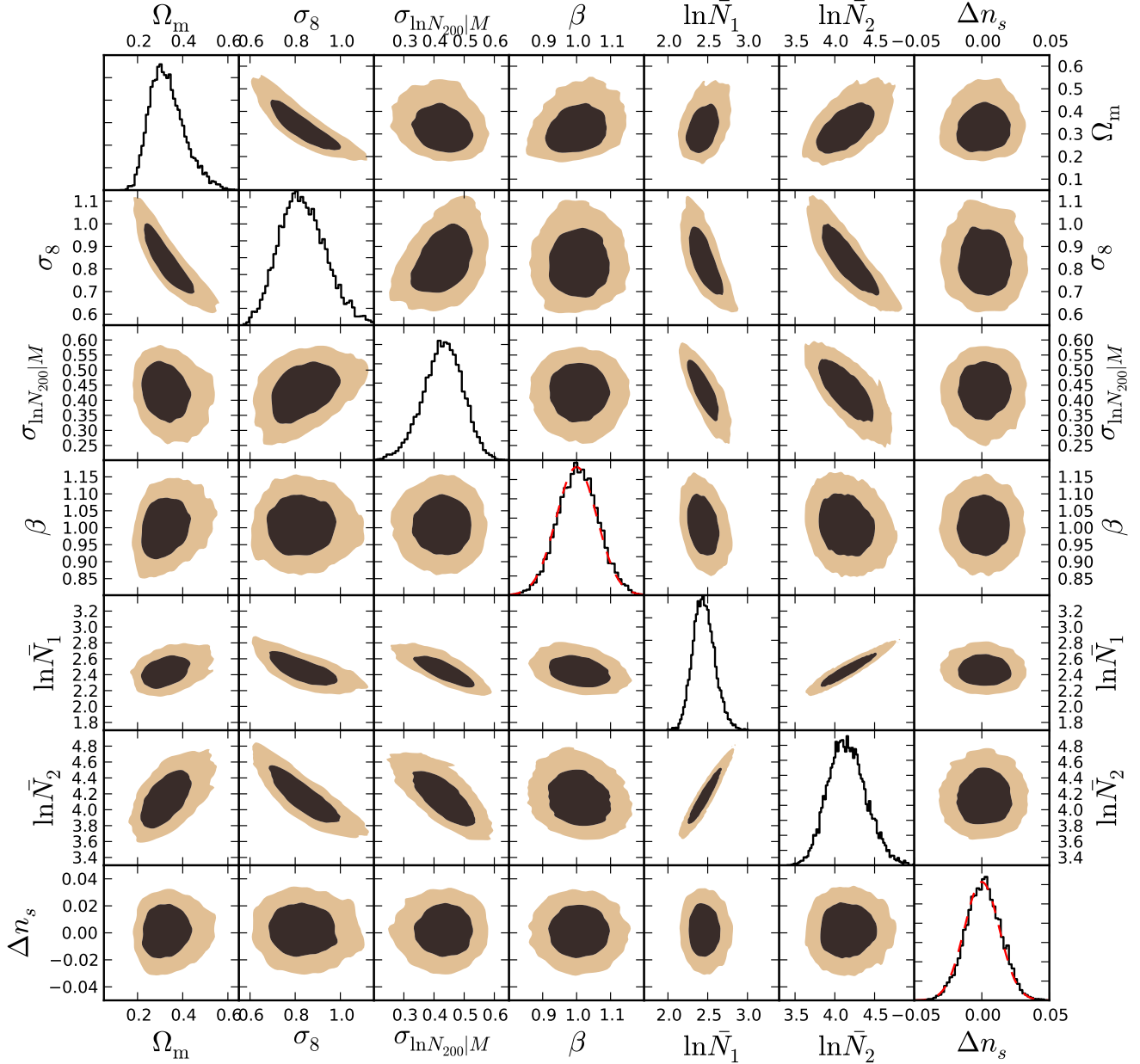


**Figure 8.** Confidence regions from our analysis of the MaxBCG data in the 2D planes that comprised of all the pair sets of model parameters. Histograms in the diagonal panels show 1D posterior distributions of individual parameters. Contour levels run through confidence limits of 95% (light brown) and 68% (dark brown) inwards. The assumed prior distributions for  $\beta$  and  $\Delta n_s$  are shown as dashed curves on the fourth and the seventh diagonal panel, respectively; they are barely distinguishable from the posterior distributions.

ilar effect on cluster number counts as increasing  $\sigma_8$ , scattering progressively more low mass halos up into each richness bin than the fiducial model. To counter this effect, the mean mass–richness relation drops in amplitude and becomes shallower, achieving a good match to the original number counts. However, the changes in  $\Delta\Sigma(R)$  are opposite to those that arise from increasing  $\sigma_8$ : because more low mass halos scatter into a given richness bin when  $\sigma_{\ln N_{200}|M}$  is higher, the amplitude of  $\Delta\Sigma(R)$  decreases despite the shift in the mean richness–mass relation, dropping on both large and small scales. The impact of increased scatter is higher at larger richness because of the steeper mass function in this regime.

For a more detailed discussion of the dependence of halo populations on  $\Omega_m$  and  $\sigma_8$ , we refer the reader to Zheng et al. (2002).

We plot representative measurements and error bars from the S09  $\Delta\Sigma(R)$  data in the middle panels, specifically the  $5h^{-1}\text{Mpc}$  and  $15h^{-1}\text{Mpc}$  points in each of the three richness bins. The impact of the (large)  $\Omega_m$  and  $\sigma_8$  changes illustrated here is significant compared to these statistical errors, and of course our full  $\Delta\Sigma(R)$  data set has six data points for each of five richness bins (see Fig. 1), with errors that are only mildly correlated. The data should thus have substantial constraining power. We can see that there is degeneracy between  $\Omega_m$  and  $\sigma_8$  as expected, but this degeneracy is partly broken by the different richness and scale dependence of the two

parameter effects. The impact of increasing the scatter  $\sigma_{\ln N_{200|M}}$  by 50% is much smaller than the impact of similar changes to the cosmological parameters, and it is strongly richness dependent, essentially vanishing for our low richness bins. We can therefore anticipate that a rather loose prior on this nuisance parameter will be enough to avoid degradation of the cosmological constraints.

The  $\Delta\Sigma(R)$  changes at  $R \leq 2h^{-1}\text{Mpc}$  effectively illustrate the origin of the R10 cosmological constraints, which use the MaxBCG number counts and the small scale (1-halo regime) weak lensing measurements. The different impact of a  $\sigma_8$  change at small and large scales shows why the index  $\gamma$  of the best constrained  $\sigma_8\Omega_m^\gamma$  combination will be higher for our analysis than for R10's.

Fig. 8 presents an overview of this paper's principal results, showing the 1D posterior distribution for each of the 7 model parameters (diagonal panels), and the 95% and 68% confidence regions for all the parameter pairs (off-diagonal panels). The prior distributions of  $\beta$  and  $\Delta n_s$  are also shown on corresponding diagonal panels. We will refer back to Fig. 7 and zoom in on different subsets of Fig. 8 multiple times in the following discussion. We are most interested, of course, on the constraints in the  $\Omega_m$ – $\sigma_8$  plane, but we must understand their dependence on other parameters.

### 5.1 Comparison to WMAP

The brown contours in the left panel of Fig. 9 show a zoom-in version of the  $\Omega_m$ – $\sigma_8$  panel from Fig. 8, marking the 68% and 95% confidence limits from our MaxBCG analysis. The error ellipses are elongated approximately along a degeneracy track of  $\sigma_8(\Omega_m/0.325)^{0.501} = 0.828 \pm 0.049$ , with the marginalized constraints  $\Omega_m = 0.325^{+0.086}_{-0.067}$  and  $\sigma_8 = 0.828^{+0.111}_{-0.097}$  ( $1\sigma$  errors). The  $\sigma_8\Omega_m^\gamma$  alignment of the error ellipses is typically seen in cluster abundance-based cosmological constraints, reflecting the counterbalancing impact of the two parameters on the halo mass function. The exact value of  $\gamma$  is contingent on cluster mass range and ancillary information used in each analysis, but it usually lies between 0.4 and 0.6.

Our results are consistent with but orthogonal to the WMAP seven-year results, which are shown as the red contours in the left panel of Fig. 9 (Komatsu et al. 2011). Our measurements pull in the direction of higher  $\Omega_m$  and  $\sigma_8$  relative to WMAP alone. The WMAP constraints rely strongly on the assumptions of the flat  $\Lambda$ CDM cosmological model to extrapolate growth from  $z = 1100$  to low redshifts. Our results are only weakly dependent on  $\Lambda$ CDM assumptions, as we are using empirical constraints on the shape of  $P(k)$  and measuring a cross-correlation that scales directly with the matter density and the low redshift amplitude of matter clustering. As with cluster mass function studies, therefore, our results can be viewed as a consistency test of the GR + cosmological constant model, one that focuses on growth of structure rather than expansion history. The joint constraints from combining the two experiments shrink the regions of equivalent confidence limits to the blue contours, yielding  $\Omega_m = 0.298^{+0.019}_{-0.020}$  and  $\sigma_8 = 0.831^{+0.020}_{-0.020}$ . The best-fit joint model is summarized in the “MaxBCG+WMAP7” column of Table 4.

### 5.2 Comparison to Other Cluster Cosmology Probes

The right panel of Fig. 9 compares the constraints from our analysis to those of two other studies using the same cluster sample, R10 and Tinker et al. (2012, hereafter Tinker12). Although using the same underlying clusters and weak lensing measurements, the

**Table 5.** Input data used in the three MaxBCG-based cosmological constraints.

	R10	Tinker12	This paper
Abundance	Yes	No	Yes
Small Scale $\Delta\Sigma(R)$	Yes	Yes	No
Large Scale $\Delta\Sigma(R)$	No	No	Yes
Other	None	Galaxy Clustering	None

three analyses are quite different from one another, as highlighted in Table 5. (Regarding the fourth row, note that galaxy clustering plays a tangential role in our analysis via the power spectrum shape prior but is central to the Tinker12 analysis.)

Using the weak lensing masses, R10 obtained constraint  $\sigma_8(\Omega_m/0.25)^{0.41} = 0.832 \pm 0.033$  (red contours in the right panel of Fig. 9). The degeneracy index  $\gamma = 0.41$  is slightly shallower than the R10 constraint because the small scale  $\Delta\Sigma(R)$  responds more strongly to  $\sigma_8$  than the large scale  $\Delta\Sigma(R)$ , as seen in the central panel of Fig. 7. The R10 errors are smaller than ours, primarily because of the higher S/N of the small scale  $\Delta\Sigma(R)$  measurements used in their analysis. It is worth emphasizing, however, that our errors are dominated by statistical errors in the  $\Delta\Sigma(R)$  data, while the R10 errors have substantial contributions from the weak lensing bias uncertainty  $\beta$  and from uncertainties on the mis-centering correlation.

The blue contours in the right panel of Fig. 9 show the constraint from Tinker12 expressed as  $\sigma_8(\Omega_m/0.290)^{0.5} = 0.863 \pm 0.048$ . Tinker12 derived constraints from measuring the mass-to-number ratio within MaxBCG clusters, therefore using the same scales of  $\Delta\Sigma(R)$  as R10. They employed additional information from Zehavi et al.'s (2011) galaxy clustering measurements, which they used to constrain the halo occupation distribution (HOD) within clusters as a function of cosmology. The dominant uncertainties in the Tinker12 error bars are systematic, from uncertainties in evolution of the galaxy luminosity function and the galaxy HOD, and from theoretical uncertainties in the halo mass function and halo bias relation.

In the right panel of Fig. 9, the three sets of contours largely overlap with each other, around the region that corresponds to the 68% confidence limit from our WMAP7 joint constraints shown in the left panel. This good agreement is encouraging, since our analysis uses different scales of  $\Delta\Sigma(R)$  and is insensitive to systematic uncertainties that affect the other two analyses. There are enough commonalities that it would be risky to combine the three constraints as though they were independent, but the agreement certainly suggests that the errors are no larger than those quoted in the individual studies. As the R10 and Tinker12 results have been shown to agree with the constraints from X-ray cluster studies, the consistency between our results and theirs expands the evidence for broad consistency between optical and X-ray studies in cluster cosmology. As statistical precision improves with larger samples (of clusters, of WL source galaxies, and of high quality X-ray measurements), these consistency tests will become considerably more stringent.

### 5.3 Constraint on the Richness–Mass Relation

For specified values of  $\Omega_m$  and  $\sigma_8$ , the statistical mass calibration in our analysis places strong constraints on the richness–mass relation. The inferred relation shifts systematically with  $\Omega_m$  and  $\sigma_8$ , as the constraint comes mainly from matching the observed richness



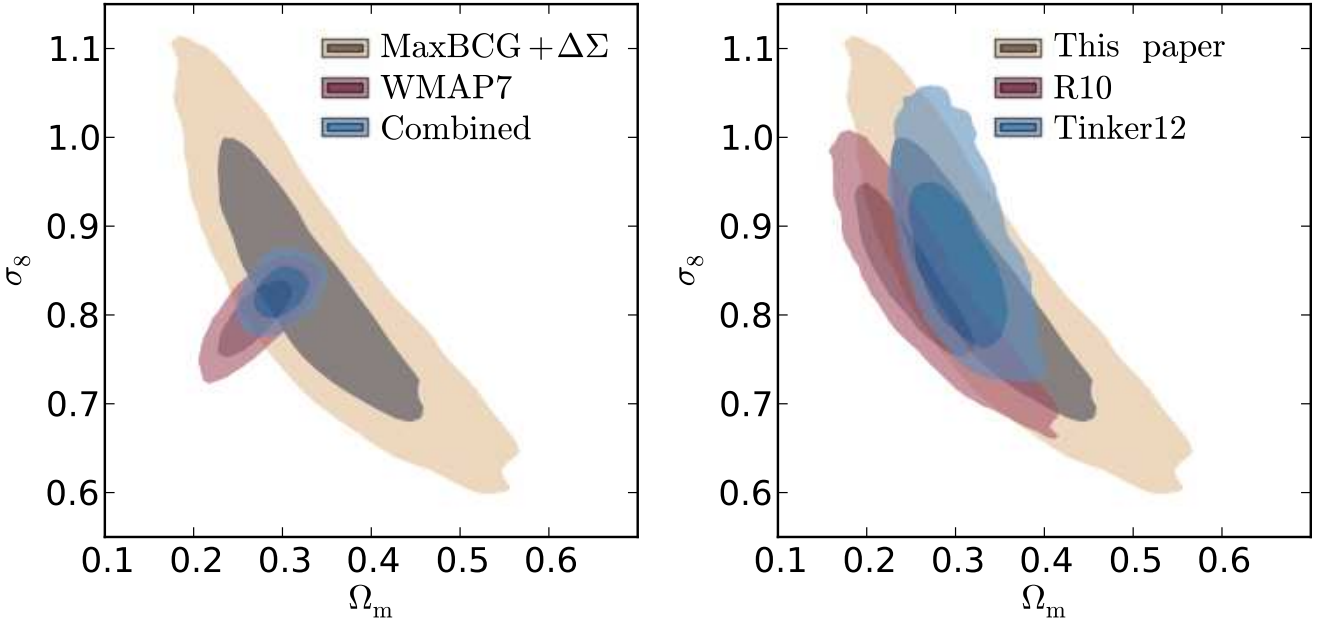


**Figure 9.** Comparison of our cosmological constraints on the  $\Omega_m$ – $\sigma_8$  plane with WMAP7 and two other studies using MaxBCG. Left: Constraints from our MaxBCG analysis (brown), WMAP7 (red), and the combination of both (blue). Right: Constraints from our analysis (brown), R10 (red), and Tinker12 (blue).

distribution given the halo mass function. The model parameters are  $\ln \bar{N}_1$  and  $\ln \bar{N}_2$ , but the constraint can be expressed in a more intuitive form by changing parameters to

$$\langle \ln N_{200} | M \rangle = A + \alpha (\ln M / M_{\text{pivot}}) \quad (18)$$

where the pivot mass is chosen to minimize correlation between the amplitude  $A$  and slope  $\alpha$ . Even for fixed cosmology, the values of  $A$  and  $\alpha$  are inevitably correlated with the scatter  $\sigma_{\ln N_{200} | M}$ , because it is the combination of the central relation and the scatter that determines the distribution of richness as a function of mass. As shown in the bottom panel of Fig. 7, one can reproduce nearly the same cluster number counts by increasing  $\sigma_{\ln N_{200} | M}$ , lowering  $A$ , and adopting a slightly shallower slope  $\alpha$ . However, the richness dependence of  $\Delta\Sigma(R)$  provides some leverage to break this degeneracy.

For the cosmological parameters and scatter of our best-fit MaxBCG+WMAP7 model, we obtain  $A = 3.233 \pm 0.020$  and  $\alpha = 0.739 \pm 0.009$  with a pivot mass  $M_{\text{pivot}} = 3.614 \times 10^{14} h^{-1} M_\odot$ , which minimizes the correlation between the two parameters. These (68%) errors are marginalized over the nuisance parameters  $\beta$  and  $\Delta n_s$ . If we also marginalize over  $\sigma_{\ln N_{200} | M}$  but use the same pivot mass, the errors increase to  $A = 3.255 \pm 0.069$  and  $\alpha = 0.744 \pm 0.016$ . We evaluate the dependence of  $A$  and  $\alpha$  on  $\Omega_m$ ,  $\sigma_8$ , and  $\sigma_{\ln N_{200} | M}$  by shifting each parameter in turn by  $\pm 10\%$  from its best-fit MaxBCG+WMAP7 value and redetermining the best-fit  $A$  and  $\alpha$  (i.e., similar to the experiments described in Fig. 7 but with smaller fractional shifts.). Our final result is

$$\begin{aligned} A &= \left( \frac{\Omega_m}{0.298} \right)^{-0.156} \left( \frac{\sigma_8}{0.831} \right)^{-0.254} \left( \frac{\sigma_{\ln N_{200} | M}}{0.426} \right)^{-0.055} \\ &\times (3.233 \pm 0.020), \\ \alpha &= \left( \frac{\Omega_m}{0.298} \right)^{-0.012} \left( \frac{\sigma_8}{0.831} \right)^{-0.446} \left( \frac{\sigma_{\ln N_{200} | M}}{0.426} \right)^{-0.135} \\ &\times (0.739 \pm 0.009), \end{aligned} \quad (19)$$

with pivot mass  $M_{\text{pivot}} = 3.614 \times 10^{14} h^{-1} M_\odot$ . Away from the fiducial values of Equation 19, the errors on  $A$  and  $\alpha$  may change, and they may become moderately correlated as the effective pivot mass drifts.

To compare to the best-fit  $\langle \ln N_{200} | M \rangle$  in R10, we scale our best-fit  $A$  and  $\alpha$  to their fiducial cosmology and scatter using the equations above, and normalize the amplitude to their  $M_{\text{pivot}} = 7.63 \times 10^{13} h_{0.7}^{-1} M_\odot$ , the best-fit values are then  $A' = 2.140$  and  $\alpha' = 0.890$ , consistent with the R10 constraints ( $A_{\text{R10}} = 2.34 \pm 0.10$  and  $\alpha_{\text{R10}} = 0.757 \pm 0.066$ ). Our richness–mass relation is rotated upward from the R10 relation by  $\simeq 4.5^\circ$  around  $3.432 \times 10^{14} h^{-1} M_\odot$ , where the two cross.

We list the average mass and bias of MaxBCG clusters in bins of richness as computed from the best-fit MaxBCG+WMAP7 joint model in Tables 1 and 2. More specifically, we take the best-fit model parameters and calculate the kernel function weighted averages via

$$\langle M_{200m} \rangle = \frac{1}{\langle N_j \rangle} \int M \omega_j(M, z) dM dz \quad (20)$$

$$\langle b \rangle = \frac{1}{\langle N_j \rangle} \int b(M, z) \omega_j(M, z) dM dz. \quad (21)$$

Note that the values of  $\langle M_{200m} \rangle$  depend on both the scatter and the slopes of the halo mass function through  $\omega_j(M, z)$ , so they are different than the “central” values from directly inverting the mean richness–mass in Equation. 18. This is most easily seen from the top panel of Fig. 2, where the actual halos inside each richness bin are mostly those with masses well below the “central” mass implied by the mean richness–mass relation for that bin. The mean halo masses are less strongly offset, as shown by the points in that panel, because the more massive clusters in the bin carry proportionally more weight. Our average cluster masses are in good agreement with the predictions from R10 (their table 2, column 3), which in turn are fits to the weak lensing masses measured in Johnston et al. (2007).

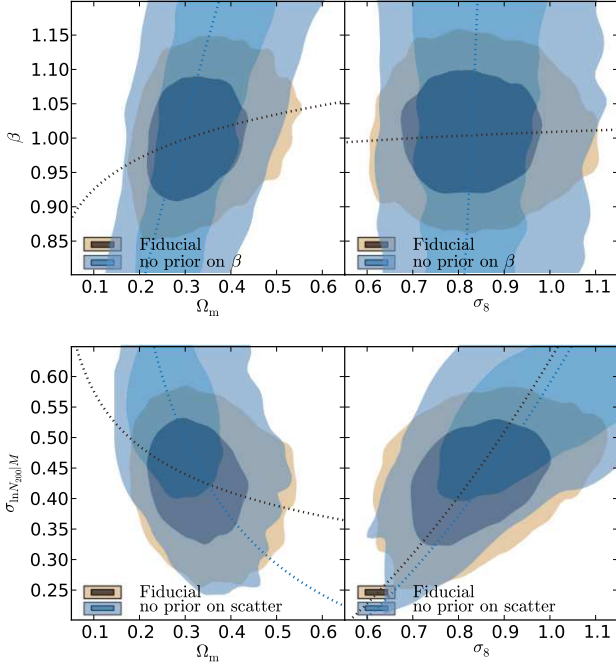


**Figure 10.** Comparison of the correlations between the cosmological parameters ( $\Omega_m$  and  $\sigma_8$ ) and the nuisance parameters ( $\sigma_{\ln N_{200}|M}$  and  $\beta$ ), before and after applying specific priors. In each panel, light and dark brown contours indicate the 68% and 95% confidence regions from our fiducial analysis, which has priors on the nuisance parameters, and blue contours show the results when there is no prior either on  $\sigma_{\ln N_{200}|M}$  (bottom panels) or on  $\beta$  (top panels). Dotted curves on top of each contour set represent the degeneracy track followed by the correlation, calculated from the eigen-decomposition of the underlying correlation matrices.

#### 5.4 Constraint on the Nuisance Parameters

As identified in Fig. 7, the main nuisance parameters in our analysis are the scatter in the richness–mass relation  $\sigma_{\ln N_{200}|M}$  and the weak lensing bias  $\beta$ , both of which are expected to correlate with the cosmological parameters. To mitigate the impact of these correlations, we have placed two Gaussian priors to help determine the ranges of  $\sigma_{\ln N_{200}|M}$  and  $\beta$ , one on the converse scatter and one directly on  $\beta$  (Table 3).

Fig. 10 compares the correlations between the two nuisance parameters ( $\sigma_{\ln N_{200}|M}$  and  $\beta$ ) and the two cosmological parameters ( $\Omega_m$  and  $\sigma_8$ ), before and after using their respective priors. As expected, when the prior on the converse scatter  $\sigma_{\ln M|N_{200}}$  is absent, we observe strong correlation between  $\sigma_{\ln N_{200}|M}$  and  $\sigma_8$ , scaling as  $\sigma_8(\sigma_{\ln N_{200}|M}/0.534)^{-0.483} = 0.953$  (blue dotted curve in the bottom right panel). The prior on  $\sigma_{\ln M|N_{200}}$  effectively eliminates the high- $\sigma_{\ln N_{200}|M}$  and high- $\sigma_8$  region and shifts the residual correlation to  $\sigma_8(\sigma_{\ln N_{200}|M}/0.432)^{-0.505} = 0.828$  (black dotted curve in the bottom right panel). Similarly, if we allow  $\beta$  to vary freely, there is correlation between  $\Omega_m$  and  $\beta$ , scaling as  $\beta(\Omega_m/0.349)^{-0.711} = 1.14$  (blue dotted curve in the top left panel), which then diminishes under the prior on  $\beta$  to  $\beta(\Omega_m/0.325)^{-0.069} = 1.0$  (black dotted curve in the top left panel). There are almost no correlations between  $\sigma_{\ln N_{200}|M}$  and  $\Omega_m$  (bottom left panel) and between  $\beta$  and  $\sigma_8$  (top right panel), either before or after imposing the priors.

The slope of the  $\Omega_m$ – $\beta$  correlation in the no prior case, however, is intriguing ( $-0.711$  as shown by the blue dotted curve in

the top left panel). Consider the experiment illustrated in the top panels of Fig. 7, where we increase  $\Omega_m$  while keeping the shape of  $P_{\text{lin}}(k)$  and the  $z = 0$  normalization  $\sigma_8$  fixed. At  $z = 0$ , the halo mass function and halo clustering of this shifted model are nearly identical to those of the original model except for an overall shift of the mass scale in proportion to  $\Omega_m$  (see Zheng et al. 2002). Once the richness–mass relation is shifted by this same constant factor, we expect a nearly identical cluster–mass correlation function at fixed richness. We therefore expect  $\Delta\Sigma(R) \propto \Omega_m \xi_{\text{cm}}$  to shift in proportion to  $\Omega_m$ , so there should be degeneracy of the form  $\beta\Omega_m^{-1} = \text{constant}$ , rather than  $\beta\Omega_m^{-0.711}$ . Our clusters have a median redshift of  $z_{\text{med}} = 0.23$  rather than zero, and the amplitude  $\sigma_8(z_{\text{med}})$  has a small dependence on  $\Omega_m$  through the linear growth factor. However, the departure from unit slope in this degeneracy arises primarily because of the dependence of volume element on  $\Omega_m$ . When  $\Omega_m$  increases the inferred volume of our cluster survey (defined by nearly fixed redshift limits and area) decreases, so the linear shift of the richness–mass relation that keeps the predicted cluster abundance fixed in comoving  $h^3\text{Mpc}^{-3}$  in fact predicts a lower number of MaxBCG clusters.

Marginalizing over all other parameters, our constraints on  $\sigma_{\ln N_{200}|M}$  and  $\beta$  are  $\sigma_{\ln N_{200}|M} = 0.432^{+0.063}_{-0.068}$  and  $\beta = 1.004^{+0.060}_{-0.060}$ , respectively, consistent with the results in R10 ( $\sigma_{\ln N_{200}|M} = 0.357 \pm 0.073$  and  $\beta = 1.016 \pm 0.060$ ). Applying WMAP7 priors tightens the constraints to  $\sigma_{\ln N_{200}|M} = 0.436^{+0.012}_{-0.024}$  and  $\beta = 0.968^{+0.034}_{-0.030}$ . As we have already commented in §5.3, there is mild tension between the scatter found here and in R10; the difference is only  $1\sigma$ , but we are using the same cluster abundance data.

#### 6 SYSTEMATIC ERRORS

We have adopted priors on several of our nuisance parameters, so there could be systematics beyond our quoted errors if these priors are too tight, or if our assumption of a power-law richness–mass relation is too restrictive.

Fig. 11 compares the 68% confidence regions in the  $\Omega_m$ – $\sigma_8$  plane derived from our fiducial analysis (filled contours) to those obtained for different priors or variations in the observational analysis (open contours).

The bottom left panel explores the robustness of our analysis against uncertainties in the scatter. When no prior on scatter is applied, the low- $\Omega_m$  and high- $\sigma_8$  regions (red solid contour) are accepted because of the degeneracy between  $\sigma_8$  and  $\sigma_{\ln N_{200}|M}$  discussed in §5.4. Our fiducial prior on the converse scatter, Gaussian with width  $\delta\sigma_{\ln N_{200}|M} = 0.10$ , makes an important difference to our individual errors on  $\Omega_m$  and  $\sigma_8$ , though it has little impact on the  $\sigma_8\Omega_m^{0.501}$  error (the degeneracy banana gets longer, not wider). If we double the prior width to  $\delta\sigma_{\ln N_{200}|M} = 0.20$  (blue contour), the cosmological constraints are close to the no prior case. However, if we halve the prior width to  $\delta\sigma_{\ln N_{200}|M} = 0.05$  (green contour), there is only modest tightening of the constraints; at the current level of statistical error in  $\Delta\Sigma(R)$ , better external knowledge of  $\sigma_{\ln N_{200}|M}$  would not make much improvement in our results. Compared to Fig. 9, we see that the additional parameter region allowed by a loose prior on scatter is ruled out if we combine with the orthogonal WMAP7 constraint. This is the reason that the posterior constraint on  $\sigma_{\ln N_{200}|M}$  is much tighter when we include WMAP7 (Table 4), even though WMAP does not probe clusters directly.

The bottom right panel of Fig. 11 tests the robustness of our

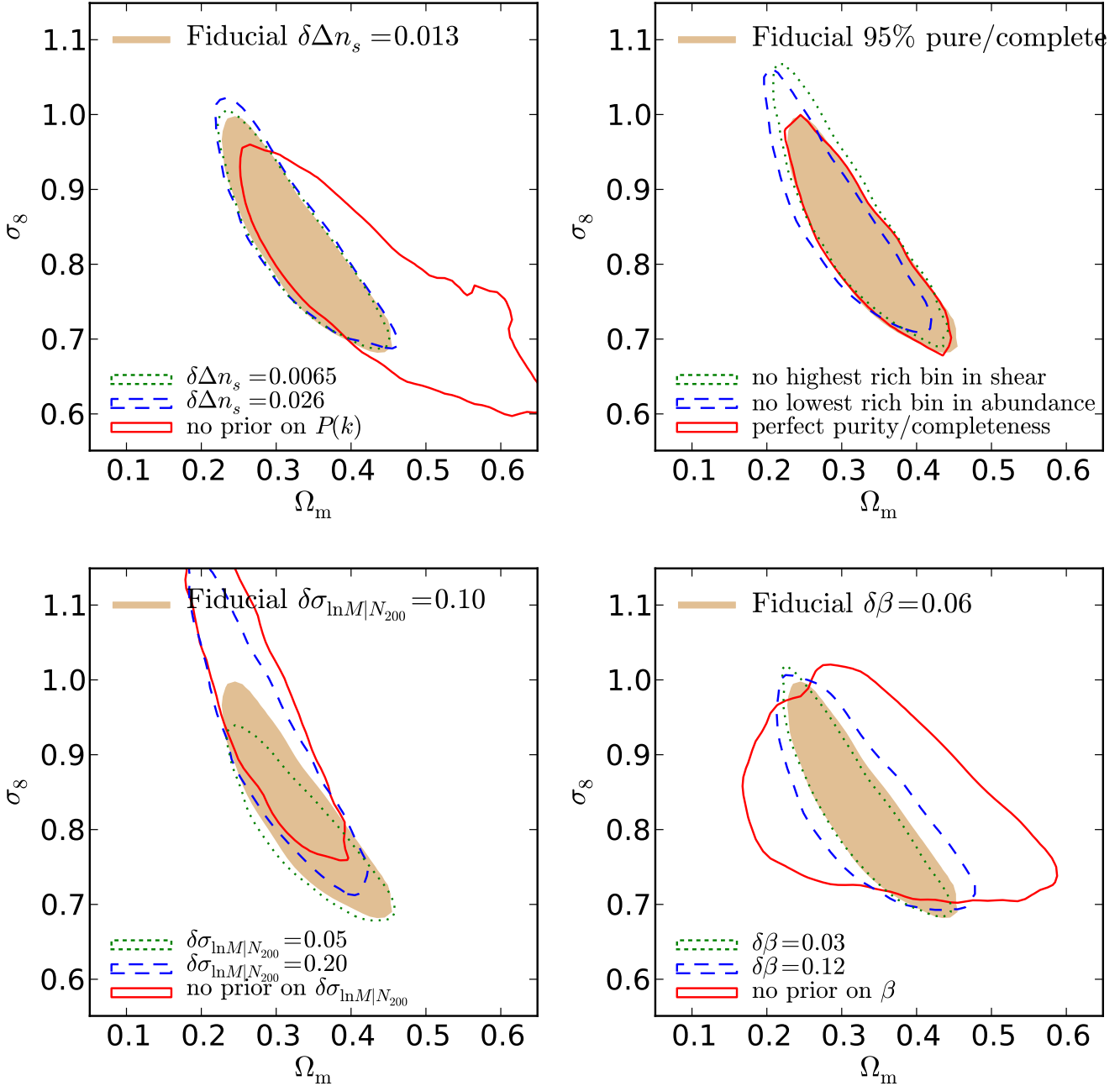


**Figure 11.** Effects of relaxing priors and varying assumptions on observational systematics on the  $\Omega_m$  and  $\sigma_8$  constraint. Contours are 68% confidence regions as constrained by our fiducial analysis (filled) or different modifications listed in each panel (open).

results against uncertainties in  $\beta$ . As discussed in § 5.4, our internal constraint on  $\beta$  comes almost entirely from the volumetric effect of  $\Omega_m$ , so we expect widening/narrowing of the Gaussian prior on  $\beta$  to have a much larger impact on  $\Omega_m$  than on  $\sigma_8$ . The blue dashed and green dotted contours show the results after we double and halve the width of the prior on  $\beta$ , respectively. The blue contour expands along the  $\Omega_m$  axis with little change along the  $\sigma_8$  axis, as anticipated. Halving the prior width produces only slight improvement in the constraints; if our fiducial prior  $\delta\beta = 0.06$  is accurate-to-conservative, as we think it is, then our constraints are limited by the statistical errors of the weak lensing measurements rather than the systematic uncertainties. If the prior on  $\beta$  is

dropped completely, i.e., we allow arbitrary rescaling of the weak lensing measurements and rely only on the relative  $\Delta\Sigma(R)$  amplitudes between bins of different richness, then the contour expands to fill nearly all possible  $\Omega_m$  ranges while showing no degradation of the constraint on  $\sigma_8$ .

The top left panel of Fig. 11 addresses the possible systematics associated with our uncertainties in the  $P(k)$  shape. The red solid contour shows the constraints on  $\Omega_m$  and  $\sigma_8$  without the  $P(k)$  shape prior. As demonstrated in § 4.3, this prior helps eliminate the physically improbable regions of high- $\Omega_m$  and low- $\sigma_8$ , which is otherwise favored due to the degeneracy between the  $P(k)$  shape and the cosmological parameters. The blue dashed and

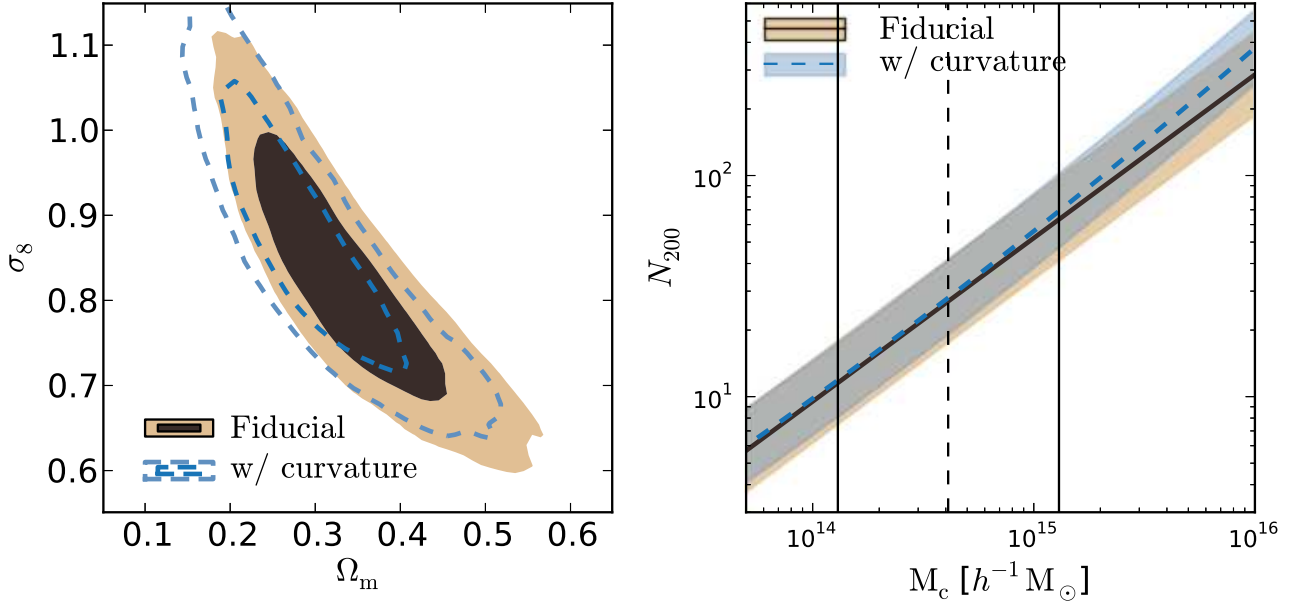


**Figure 12.** Effects of allowing curvature in the richness–mass relation on the  $\Omega_m$  and  $\sigma_8$  constraint (left) and the best-fit curved richness–mass relation (right). Left: comparison of the 68% and 95% confidence regions derived from the fiducial (filled) and the curved model (open). Right: The best-fit power-law (thick solid line) and piecewise spline interpolated (thick dashed curve) mean richness–mass relations. The gray band and the thin dashed curves indicate the scatter about the mean relations. The two solid vertical lines indicate  $M_1$  and  $M_2$ , while the dashed line indicates the additional tensor point  $M_3$  for the model with curvature.

green dotted contours represent the 68% confidence regions after increasing and decreasing the width of the Gaussian prior on  $\Delta n_s$  by factor of two, respectively. Both contours barely differ from the fiducial result, indicating our constraints on  $\Omega_m$ – $\sigma_8$  are robust against the uncertainties in the tilt of the primordial power spectrum within the range allowed by galaxy surveys.

In the top right panel of Fig. 11, we examine the robustness of our constraint against the uncertainties in the completeness and purity level of the sample and its sensitivity to the  $\Delta\Sigma(R)$  measurements in the extreme richness clusters. As discussed in §3.2.2, we allow for potential biases related to incompleteness or contamination by adding  $\text{Var}(\lambda) = 0.05^2$  to all elements of our covariance matrix, diagonal and off-diagonal, based on estimates that the MaxBCG catalog is at least 95% complete and pure in our richness range. The red contour shows the effect of dropping this contribution to the covariance matrix, which is negligible. We conclude that uncertainties in completeness and contamination at the 5% level do not affect our constraints.

For the richness dependence of  $\lambda$ , it is known that low richness clusters are subject to a higher rate of contamination than rich clusters, so we try our analysis excluding the number count datum for the lowest richness bin at  $N_{200} \in [11 - 15]$ . The result is shown as the blue dashed contour, which drifts up from the fiducial one approximately along the degeneracy track. The constraints from the blue dashed contour are  $\sigma_8(\Omega_m/0.293)^{0.489} = 0.863 \pm 0.049$ , which slightly torques the halo mass function to better fit the cluster richness function beyond the lowest bin. Since the abundance error is smallest for our lowest richness bin, it carries significant weight in the analysis, so it can have a noticeable impact even though it is only one of nine abundance data points. However, the drift of the contour is small compared to its size, so even contamination

at the 5% level in this bin would affect our result at a level small compared to the statistical error.

As for the stacked  $\Delta\Sigma(R)$  measurements, the largest uncertainty occurs at the highest richness bin where the total number of source galaxies is the least. The green dotted contour shows the effect of removing the highest richness bin in the  $\Delta\Sigma(R)$  measurements. The resulting confidence region elongates to accept some high- $\sigma_8$  regions, because despite being noisy, the highest richness bin carries more  $\sigma_8$ -sensitive information than other bins.

Although the average mapping between the true mass and optical richness of clusters should be monotonic, a power-law may be an over-simplification. To allow curvature in the mapping, we add a third parameter in the mean richness–mass relation as the mean log-richness  $\ln \bar{N}_3$  at  $M_3 = 4.1 \times 10^{14} h^{-1} M_\odot$  (i.e., the geometric mean of  $M_1$  and  $M_2$ ), then we spline interpolate through the three tensor points on the log-mass vs. log-richness plane for any given  $\ln \bar{N}_1$ ,  $\ln \bar{N}_2$ , and  $\ln \bar{N}_3$ , to find a smooth curve that represents the new mean richness–mass relation. Fig. 12 shows the results of adding curvature at  $M_3$ . Similar to the test where we dropped the lowest richness bin in § 6, the confidence regions slide up along the degeneracy track for a gentle torque in the halo mass function (blue open contours in the left panel), and the richness–mass relation bends slightly (blue dashed curve in the right panel) to reduce the number of the highest richness clusters. In this way, the model achieves a better fit to the detailed shape of the observed richness function than the fiducial power-law model. However, the best-fit curved richness–mass relation remains very close to a power law over the relevant mass range, and the parameter constraints shift only slightly relative to the fiducial ones. The width of the constraints grows only small amount, indicating that our assumption of a power-law relation in our fiducial analysis does not bias or overly restrict our results.

## 7 SUMMARY AND FUTURE PROSPECTS

We have derived cosmological constraints on  $\Omega_m$  and  $\sigma_8$  using the combination of large scale cluster–galaxy weak lensing measurements (S09) and the abundance of MaxBCG clusters as a function of richness. Within the analysis, we have statistically calibrated the cluster masses by requiring consistency between the cosmological model fit and the data, exploiting external priors on the scatter in the richness–mass relation from comparisons to X-ray data (Rozo et al. 2009), and on the  $P(k)$  shape from galaxy clustering Reid et al. (2010). The 68% confidence ellipse of our cosmological constraints on the  $\Omega_m$ – $\sigma_8$  plane can be summarized as

$$\sigma_8(\Omega_m/0.325)^{0.501} = 0.828 \pm 0.049, \quad (22)$$

which is consistent with and orthogonal to the WMAP7 constraints on these parameters. This consistency of structure measured in the recombination era and the low redshift universe provides further evidence for the gravitational growth predicted by the  $\Lambda$ CDM model combining GR, a cosmological constant, and cold dark matter. Assuming this model to be correct and combining our analysis with WMAP7, we obtain individual constraints as

$$\Omega_m = 0.298 \pm 0.020 \quad \text{and} \quad \sigma_8 = 0.831 \pm 0.020. \quad (23)$$

The overall results are consistent with and complementary to two other cosmological constraints from the same underlying clusters but with different input data and systematic uncertainties (R10 and Tinker12). Collectively these three studies demonstrate consistency of the small scale weak lensing, large scale weak lensing, galaxy content, and abundance of the MaxBCG sample, together with galaxy clustering data.

The primary systematic uncertainties in our analysis are the scatter in the cluster richness–mass relation and residual bias in the weak lensing measurements associated with photometric redshifts or shear calibration. However, with the external priors we have adopted, neither of these systematics is a limiting factor in our analysis; the uncertainties in our cosmological constraints are dominated by statistical uncertainties in the large scale  $\Delta\Sigma(R)$  measurements. These statistical errors can be sharply reduced in future surveys with deeper imaging and better seeing. Statistical improvements will require corresponding improvements in the control of systematics. While we have focused in this paper on large scales to complement the R10 analysis, the long term goal should be to derive constraints from the full range of  $\Delta\Sigma(R)$  simultaneously. Achieving this goal will require theoretical and numerical work to construct models that are accurate across the 1-halo and 2-halo transition and to assess uncertainties in the accuracy of the model predictions at all scales.

There are opportunities for significant near-term improvements in our analysis using SDSS data. The MaxBCG catalog and weak lensing measurements used here are based on imaging data from DR4. With the recent release of DR8 (Aihara et al. 2011), almost every aspect of the catalog construction and the weak lensing measurements has evolved. The increase in the imaging area will enhance the raw statistical power (for 7,398 deg<sup>2</sup> vs. 14,555 deg<sup>2</sup>), reducing Poisson uncertainties and sample variance in the cluster counts and shape noise in the  $\Delta\Sigma(R)$  measurements. The optical cluster finding algorithm has been improved to produce catalogs with well-controlled selection function and, more importantly, a new richness estimator with reduced intrinsic scatter. Rykoff et al. (2012) considered various modifications of the original richness estimator in MaxBCG and found that the scatter in log-mass at fixed richness could be reduced to 0.2 – 0.3 depending on

richness, substantially smaller than MaxBCG scatter ( $0.45 \pm 0.10$ ; Rozo et al. 2009) that we adopted as a prior in our analysis. When the scatter itself is smaller, then the systematic uncertainty tied to uncertainty in the scatter is also smaller. With improved uncertainty of the selection function, it will be feasible to use higher redshift clusters in the analysis, and while the  $\Delta\Sigma(R)$  measurements will degrade at higher  $z$  because of reduced source surface density, the leverage of a wider redshift range may strengthen the cosmological constraints. On the weak lensing side, the main improvement is a better understanding of the photometric redshift distribution of source galaxies. With a much improved spectroscopic training set and better photometric calibration, Sheldon et al. (2011) reconstructed a redshift distribution for DR8 imaging data that is primarily limited by sample variance. Additional improvements come from updates in the photometric pipeline, including better sky subtraction, more refined stellar masks, and better PSF corrections in the shape measurements.

Beyond SDSS, our approach can be applied to future, deeper, large-area imaging surveys. In the near term, the Pan-STARRS1 (PS1; Chambers 2007)  $3\pi$  survey is expected to have larger area than SDSS, slightly greater depth, and higher image quality that yields a significant increase of the source density for weak lensing. The Dark Energy Survey (DES; Collaboration 2005), expected to start in late 2012, plans to survey 5000 deg<sup>2</sup> to a depth two magnitudes beyond SDSS, with a weak lensing source density a factor of ten higher. It is designed with cluster cosmology and weak lensing as central goals, and our technique is naturally adapted to it. In the longer term, the imaging data sets from LSST, and the Euclid and WFIRST missions will allow radical improvements in the precision of cluster–galaxy lensing analysis, with effective source densities of 20 – 40 arcmin<sup>−2</sup>. These imaging surveys can provide their own cluster catalogs identified from the galaxy population, and they can provide stacked weak lensing measurements for clusters identified via X-ray emission or the SZ effect. Comparisons of results from different classes of cluster catalogs allow powerful cross-checks for systematics (see, e.g., Rozo et al. 2012a,b,c) and valuable constraints on mass–observable relations (Cunha & Evrard 2010). The SZ effect is a powerful technique for finding massive clusters at very high redshifts (e.g., Reichardt et al. 2012; Williamson et al. 2011; Marriage et al. 2011), and DES will target the area covered by the SZ survey of the South Pole Telescope. X-ray observables may be more tightly correlated with halo mass than optical observables, and the upcoming eROSITA mission will carry out a sensitive all-sky X-ray survey that will revolutionize cosmological studies with X-ray selected clusters.

Oguri & Takada (2011) and Weinberg et al. (2012) argue that cluster abundances with masses calibrated by stacked weak lensing can provide constraints on structure growth that are highly competitive with those from cosmic shear analysis of the same WL survey. This conclusion assumes  $\Delta\Sigma(R)$  measurements out to  $\sim 1 - 2$  cluster virial radii, so the larger scale analysis illustrated here can only strengthen the power of this approach. Cluster–galaxy lensing is analogous to galaxy–galaxy lensing, but the relation between clusters and halos is simpler than the relation between galaxies and halos, and it is less subject to the complexities of baryonic physics. This greater simplicity reduces systematic uncertainty associated with theoretical modeling, which may ultimately compensate for the rarity of clusters relative to galaxies (and consequent lower statistical precision of the WL measurements). The Tinker12 study shows that the constraining power of small scale measurements can be enhanced by bringing in additional information from galaxy



clustering and cluster mass-to-number ratios. In future work, we will investigate the generalization of this idea to large scales using the cluster-galaxy cross-correlation function, which can be measured in projection from the same survey used for weak lensing analysis. Nature has provided observable signposts that mark the locations of the most massive halos in the universe, and stacked weak lensing provides a tool to measure the average mass profiles of these halos at high precision over a wide range of scales. Exploiting this combination promises to yield stringent tests of gravity on cosmological scales and of theories for the origin of cosmic acceleration.

## ACKNOWLEDGEMENTS

We thank Anatoly Klypin for providing the L1000W simulation. D.H.W. and Y.Z. are supported by the NSF grant AST-1009505. E.R. is funded by NASA through the Einstein Fellowship Program, grant PF9-00068. M.R.B. is supported in part by the Kavli Institute for Cosmological Physics at the University of Chicago through grants NSF PHY-0114422 and NSF PHY-0551142, and an endowment from the Kavli Foundation and its founder Fred Kavli.

Funding for the SDSS and SDSS-II has been provided by the Alfred P. Sloan Foundation, the Participating Institutions, the National Science Foundation, the U.S. Department of Energy, the National Aeronautics and Space Administration, the Japanese Monbukagakusho, the Max Planck Society, and the Higher Education Funding Council for England. The SDSS Web Site is <http://www.sdss.org/>.

The SDSS is managed by the Astrophysical Research Consortium for the Participating Institutions. The Participating Institutions are the American Museum of Natural History, Astrophysical Institute Potsdam, University of Basel, University of Cambridge, Case Western Reserve University, University of Chicago, Drexel University, Fermilab, the Institute for Advanced Study, the Japan Participation Group, Johns Hopkins University, the Joint Institute for Nuclear Astrophysics, the Kavli Institute for Particle Astrophysics and Cosmology, the Korean Scientist Group, the Chinese Academy of Sciences (LAMOST), Los Alamos National Laboratory, the Max-Planck-Institute for Astronomy (MPIA), the Max-Planck-Institute for Astrophysics (MPA), New Mexico State University, Ohio State University, University of Pittsburgh, University of Portsmouth, Princeton University, the United States Naval Observatory, and the University of Washington.

## REFERENCES

- Adelman-McCarthy J. K. et al., 2006, *The Astrophysical Journal Supplement Series*, 162, 38
- Aihara H. et al., 2011, *The Astrophysical Journal Supplement Series*, 193, 29
- Allen S. W., Evrard A. E., Mantz A. B., 2011, 53
- Burenin R. A., Vikhlinin A., Hornstrup A., Ebeling H., Quintana H., Mescheryakov A., 2007, *The Astrophysical Journal Supplement Series*, 172, 561
- Chambers K. C., 2007, in , p. 995
- Collaboration T. D. E. S., 2005, *The dark energy survey*
- Cooray A., Sheth R., 2002, *Physics Reports*, 372, 1
- Cunha C. E., Evrard A. E., 2010, *Physical Review D*, 81, 83509
- Dodelson S., 2004, *Physical Review D*, 70, 23008
- Eisenstein D. J., Hu W., 1999, *The Astrophysical Journal*, 511, 5–15
- George M. R. et al., 2012, *arXiv:1205.4262*
- Gottloeber S., Klypin A., 2008, *The ART of cosmological simulations*
- Hayashi E., White S. D. M., 2008, *Monthly Notices of the Royal Astronomical Society*, 388, 2–14
- Hoekstra H., Hartlap J., Hilbert S., van Uitert E., 2011, *Monthly Notices of the Royal Astronomical Society*, 412, 2095
- Hu W., Kravtsov A. V., 2003, *The Astrophysical Journal*, 584, 702–715
- Johnston D. E. et al., 2007
- Koester B. P. et al., 2007, *The Astrophysical Journal*, 660, 239
- Komatsu E. et al., 2011, *The Astrophysical Journal Supplement Series*, 192, 18
- Kravtsov A. V., Klypin A. A., Khokhlov A. M., 1997, *The Astrophysical Journal Supplement Series*, 111, 73
- Mandelbaum R. et al., 2008, *Monthly Notices of the Royal Astronomical Society*, 386, 781
- Marriage T. A. et al., 2011, *The Astrophysical Journal*, 737, 61
- Miralda-Escude J., 1991, *The Astrophysical Journal*, 370, 1
- Navarro J. F., Frenk C. S., White S. D. M., 1996, *The Astrophysical Journal*, 462, 563
- Oguri M., Takada M., 2011, *Physical Review D*, 83, 29
- Prada F., Klypin A. A., Cuesta A. J., Betancort-Rijo J. E., Primack J., 2012, *Monthly Notices of the Royal Astronomical Society*, 3206
- Reichardt C. L. et al., 2012, *Galaxy clusters discovered via the Sunyaev-Zel'dovich effect in the first 720 square degrees of the south pole telescope survey*
- Reid B. A. et al., 2010, *Monthly Notices of the Royal Astronomical Society*, 404, 60–85 (Reid10)
- Rozo E., Bartlett J. G., Evrard A. E., Rykoff E. S., 2012a, *arXiv:1204.6305*
- Rozo E., Evrard A. E., Rykoff E. S., Bartlett J. G., 2012b, *arXiv:1204.6292*
- Rozo E., Rykoff E. S., Bartlett J. G., Evrard A. E., 2012c, *arXiv:1204.6301*
- Rozo E. et al., 2009, *The Astrophysical Journal*, 699, 768
- Rozo E., Wechsler R. H., Koester B. P., Evrard A. E., McKay T. A., 2007a, 19
- Rozo E. et al., 2007b
- Rozo E. et al., 2010, *The Astrophysical Journal*, 708, 645–660 (R10)
- Rykoff E. S. et al., 2012, *The Astrophysical Journal*, 746, 178
- Sanderson A. J. R., Edge A. C., Smith G. P., 2009, *Monthly Notices of the Royal Astronomical Society*, 398, 1698
- Sheldon E. et al., 2009, *The Astrophysical Journal*, 703, 2217 (S09)
- Sheldon E. S., Cunha C., Mandelbaum R., Brinkmann J., Weaver B. A., 2011, *Photometric redshift probability distributions for galaxies in the SDSS DR8*
- Sheldon E. S. et al., 2004, *The Astronomical Journal*, 127, 2544–2564
- Smith R. E. et al., 2003, *Monthly Notices of the Royal Astronomical Society*, 341, 1311–1332
- Sunyaev R. A., Zeldovich Y. B., 1972, *Comments on Astrophysics and Space Physics*, 4, 173
- Tinker J., Kravtsov A. V., Klypin A., Abazajian K., Warren M., Yepes G., Gottlöber S., Holz D. E., 2008, *The Astrophysical Journal*, 688, 709–728
- Tinker J. L., Robertson B. E., Kravtsov A. V., Klypin A., Warren M. S., Yepes G., Gottlöber S., 2010, *The Astrophysical Journal*, 724, 878–886
- Tinker J. L. et al., 2012, *The Astrophysical Journal*, 745, 16 (Tinker12)
- Vikhlinin A. et al., 2009, *The Astrophysical Journal*, 692, 1060–1074
- Weinberg D. H., Mortonson M. J., Eisenstein D. J., Hirata C., Riess A. G., Rozo E., 2012, *Observational probes of cosmic acceleration*
- Williamson R. et al., 2011, *The Astrophysical Journal*, 738, 139
- York D. G. et al., 2000, *The Astronomical Journal*, 120, 1579
- Zehavi I. et al., 2011, *The Astrophysical Journal*, 736, 59
- Zhao D. H., Jing Y. P., Mo H. J., Börner G., 2009, *The Astrophysical Journal*, 707, 354–369
- Zheng Z., Tinker J. L., Weinberg D. H., Berlind A. A., 2002, *The Astrophysical Journal*, 575, 617